

Electronic Thesis and Dissertation Repository

---

9-22-2020 10:00 AM

## Theoretical Investigation of Pressure-Induced Structural Transformations of Ethylenediamine Bisborane

Rongfeng Guan, *The University of Western Ontario*

Supervisor: Staroverov, Viktor N., *The University of Western Ontario*

: Song, Yang, *The University of Western Ontario*

A thesis submitted in partial fulfillment of the requirements for the Master of Science degree in Chemistry

© Rongfeng Guan 2020

Follow this and additional works at: <https://ir.lib.uwo.ca/etd>

 Part of the [Physical Chemistry Commons](#)

---

### Recommended Citation

Guan, Rongfeng, "Theoretical Investigation of Pressure-Induced Structural Transformations of Ethylenediamine Bisborane" (2020). *Electronic Thesis and Dissertation Repository*. 7372.  
<https://ir.lib.uwo.ca/etd/7372>

This Dissertation/Thesis is brought to you for free and open access by Scholarship@Western. It has been accepted for inclusion in Electronic Thesis and Dissertation Repository by an authorized administrator of Scholarship@Western. For more information, please contact [wlsadmin@uwo.ca](mailto:wlsadmin@uwo.ca).

## Abstract

High-pressure experiments on hydrogen-rich compounds provide crucial data for the rational design of hydrogen storage materials. Ethylenediamine bisborane (EDAB),  $\text{BH}_3 \cdot \text{NH}_2\text{CH}_2\text{CH}_2\text{NH}_2 \cdot \text{BH}_3$ , is one of the prime candidates for this role due to its high hydrogen content (10 wt%) and good kinetic stability under ambient conditions. Previous studies of EDAB using *in situ* Fourier-transform infrared (IR) spectroscopy, Raman spectroscopy, and synchrotron X-ray diffraction (XRD) techniques suggested that EDAB undergoes two possible phase transitions in the pressure range of 0 to 17 GPa. However, the crystal structures of the two new phases arising in these transitions remained unknown due to experimental challenges of *in situ* structural characterization under high pressures. In this study, we perform Kohn–Sham density functional theory (DFT) calculations and identify the structures of the two high-pressure phases of EDAB. Our results confirm that EDAB undergoes two structural transformations. The first one is at 1 GPa from the orthorhombic *Pbca* ambient-pressure structure (phase I) to the monoclinic *P2<sub>1</sub>/c* structure (phase II). The second is at 8 GPa from phase II to another structure (phase III) of the monoclinic *P2<sub>1</sub>/c* symmetry, which remains the dominant phase up to at least 17 GPa. The mechanism of these phase transitions is attributed to the formation of dihydrogen bonding frameworks, revealed by DFT calculations.

**Keywords:** hydrogen storage materials, density-functional theory, pressure-induced polymorphic transformation, ethylenediamine bisborane, dihydrogen bonds, X-ray diffraction

## Summary for Lay Audience

Hydrogen-rich chemical compounds have long attracted attention as efficient carriers of elemental hydrogen—a renewable and environmentally friendly potential replacement for fossil fuels. Because hydrogen uptake and release by these compounds is controlled by varying temperature and pressure, it is essential to understand how they behave under compression. Several specific compounds that can store and release hydrogen have been proposed and investigated so far. One of them, called ethylenediamine bisborane (EDAB), was studied by Dr. Song's group at Western using optical spectroscopies and X-ray diffraction techniques. The experimental observations suggested that EDAB undergoes two possible structural changes when the pressure rises from atmospheric to 17 gigapascals (GPa). However, the crystal structures of those two new phases could not be determined due to the challenges of interpreting the experimental data. In this work, we performed quantum-mechanical calculations to identify the crystal structures of two new high-pressure phases of EDAB. We confirmed that EDAB undergoes two transformations near 1 and 8 GPa, respectively, and determined their crystal structures. Our calculations also shed light on how the molecules of EDAB re-orient themselves under applied pressure. These findings contribute to the fundamental understanding of the high-pressure chemistry of EDAB and will help the development of new hydrogen storage materials.

## **Co-Authorship Statement**

In chapters 1 and 4, the experimental XRD and cell parameters of EDAB were obtained by Pan Wang. Rongfeng Guan carried out all the calculations and wrote the draft. Dr. Viktor N. Staroverov and Dr. Yang Song edited the content.

In chapters 2, 3, 4 and 5, all the calculations were carried out by Rongfeng Guan. The calculated results were concluded and written by Rongfeng Guan. Dr. Viktor N. Staroverov and Dr. Yang Song edited the content.

All the calculations in this thesis were performed on SHARCNET and WestGrid, COMPUTE CANADA.

## **Acknowledgements**

I would like to express my deepest gratitude to Prof. Staroverov and Prof. Song for their patient guidance in the past two years. While under their supervision, I learned to think scientifically. Without their encouragement and inspiration, I would not have completed my work successfully. They gave me a memorable experience in Canada and I am very glad I have been working with them! This is an experience I will treasure for the rest of my life.

I would also like to thank sincerely my lab colleagues, Amer El-Samman, Liyuan Ye, Nicholas Hoffman, and Tiantian Mi for all their assistance throughout this project. Work runs smoothly when you study in a collaborative and supportive environment. I also acknowledge Pan Wang and Boqing Li for the wonderful discussion of experimental data analysis.

Finally, I greatly appreciate the support from my parents. They have always encouraged me on my road of chasing dreams.

# Contents

<b>Abstract.....</b>	<b>ii</b>
<b>Summary for Lay Audience.....</b>	<b>iii</b>
<b>Co-Authorship Statement .....</b>	<b>iv</b>
<b>Acknowledgements .....</b>	<b>v</b>
<b>List of Figures.....</b>	<b>viii</b>
<b>List of Tables .....</b>	<b>ix</b>
<b>List of Abbreviation.....</b>	<b>x</b>
<b>1 Introduction .....</b>	<b>1</b>
1.1 High-pressure materials science and technology .....	1
1.2 Hydrogen storage materials.....	5
1.3 Overview of computational methods for materials at high pressures .....	8
1.4 Scope of this study .....	12
<b>2 Computational methodology .....</b>	<b>15</b>
2.1 Kohn–Sham density functional theory .....	15
2.1.1 LDA functional.....	16
2.1.2 PBE functional.....	17
2.1.3 PBEsol functional.....	18
2.1.4 Van der Waals density functional.....	18
2.2 Periodic structures and plane waves.....	19
2.3 <b>k</b> -point mesh in Brillouin zone.....	19
2.4 Kinetic energy cutoff.....	20
2.5 Pseudopotentials.....	21
2.6 Evolutionary prediction of high-pressure structures .....	23
2.7 Summary of the optimized methodology for crystal-structure calculations .....	24
2.7.1 Convergence testing calculations .....	24
2.7.2 Selection of density functionals.....	26
2.7.3 Selection of pseudopotentials .....	27
<b>3 Generation of candidate structures .....</b>	<b>28</b>

3.1	Lattice parameter prediction at ambient pressures .....	28
3.2	Generation of candidate structures using USPEX.....	30
<b>4</b>	<b>Identification of the new high-pressure phases of EDAB .....</b>	<b>32</b>
4.1	Pressure-enthalpy curves of EDAB candidates using the vdW-DF and PBE functionals	32
4.2	Comparison between experimental and simulated XRD patterns.....	37
4.3	Equation of state for EDAB .....	41
<b>5</b>	<b>Evolution of dihydrogen bonding frameworks in EDAB .....</b>	<b>43</b>
5.1	The dihydrogen bonding frameworks of phase II .....	43
5.2	The dihydrogen bonding frameworks of phase III.....	46
5.3	The origin of the phase transformations in EDAB at high pressure .....	47
<b>6</b>	<b>Summary and outlook .....</b>	<b>48</b>
	<b>Bibliography .....</b>	<b>49</b>
	<b>Appendix.....</b>	<b>63</b>
	<b>Curriculum Vitae.....</b>	<b>65</b>

# List of Figures

Figure 1.1: Quantum mechanics description of high-pressure effects.....	2
Figure 1.2: Novel materials discovered through high-pressure studies.....	2
Figure 1.3: The schematic drawing of a diamond anvil cell.....	4
Figure 1.4: The dihydrogen bonding framework between $\text{NH}_3\text{BH}_3$ molecules .....	8
Figure 1.5: The unit cell of EDAB at ambient pressure .....	13
Figure 1.6: Synchrotron XRD patterns of EDAB under compression at room temperature .....	14
Figure 2.1: The norm-conserving pseudopotential of carbon.....	22
Figure 2.2: All electron and pseudopotential wave functions.....	23
Figure 2.3: Structure optimization calculations of EDAB performed using the PBE functional. ....	25
Figure 3.1: Crystal structures of the seven top-ranked candidates at ambient pressure. ....	31
Figure 4.1: Calculated vdW-DF enthalpies of the seven candidate structures versus pressure....	33
Figure 4.2: Calculated PBE enthalpies of the seven candidate structures versus pressure.....	34
Figure 4.3: The simulated and experimental XRD spectra of the $P2_1/c$ (A) structure .....	37
Figure 4.4: The simulated and experimental XRD spectra of the $P2_1/c$ (A) and the $P2_1/c$ (B) structures. ....	38
Figure 4.5: Equation of state for the EDAB phases.....	42
Figure 5.1: Dihydrogen bonding frameworks between EDAB molecules at 2 GPa and 8 GPa... ..	44
Figure 5.2: The N-H...H-B distance, the N-H...H and B-H...H angles versus pressure in phase II .....	45
Figure 5.3: The N-H...H-B distance, the N-H...H and B-H...H angles versus pressure in phase III.....	46



## List of Tables

Table 1.1: Computational studies of hydrogen storage materials at high pressures .....	7
Table 1.2: Computational packages applied to high-pressure materials science.....	10
Table 2.1: Comparison of the lattice parameters of EDAB optimized using four functionals .....	26
Table 2.2: Comparison of the lattice parameters of EDAB optimized using the USPP and PAW pseudopotentials.....	27
Table 3.1: Possible lattice parameters of phase II generated using DICVOL .....	29
Table 3.2: Possible lattice parameters of phase III generated using DICVOL.....	30
Table 4.1: Relative enthalpies as a function of pressure for seven candidate structures calculated using the vdW-DF functional.....	35
Table 4.2: Relative enthalpies as a function of pressure for seven candidate structures calculated using the PBE functional .....	36
Table 4.3: Experimental unit cell parameters of EDAB as a function of pressure .....	39
Table 4.4: Computational unit cell parameters of EDAB as a function of pressure.....	40
Table 4.5: Comparison of experimental and computational data of equation of state in EDAB .	42
Table 5.1: Bond lengths of covalent N-H, B-H and C-H in EDAB molecules under high pressure .....	47

## List of Abbreviation

DFT	density functional theory
DHB	dihydrogen bond
EDAB	ethylenediamine bisborane
GGA	generalized gradient approximation
IR	infrared
LDA	local density approximation
MARE	mean absolute relative error
PBE	Perdew–Burke–Ernzerhof
PBEsol	Perdew–Burke–Ernzerhof for solids
USPP	ultrasoft pseudopotential
vdW-DF	van der Waals density functional
XRD	X-ray diffraction

1 hartree = 27.211386 eV

1 rydberg = 1/2 hartree

# 1 Introduction

## 1.1 High-pressure materials science and technology

As a physical parameter and a fundamental thermodynamic variable, pressure has one of the largest ranges in the universe, spanning over 60 orders of magnitude from  $10^{-32}$  atmosphere (atm) pressure in intergalactic space to  $10^{28}$  atm at the center of neutron stars. When materials are subjected to extremely high pressures, they can exhibit substantial changes in chemical bonding, giving rise to novel phases and new chemical reactions not observed under the atmospheric pressure [1–12]. Recently, the science of high-pressure materials has become an active research area that inspires scientists to explore the limits of our knowledge of matter.

High pressure can effectively shorten the inter-molecular and intra-molecular bond lengths in materials. According to quantum mechanics, mechanical compression of chemical bonds reduces the space available to the electrons and steeply increases their kinetic energy [13–15]. Figure 1.1a illustrates such a scenario of the electronic energy evolution as a function of bond length changes induced by high pressures, while Fig 1.1b shows the buildup of electron density between atoms caused by high pressure. This suggests that new classes of materials with novel properties can be generated by applying high pressure. For instance, polymeric nitrogen, a potential high-energy-density material, can be formed from  $N_2$  molecules by the destabilization of one nitrogen triple bond to three single bonds under high pressure and temperature [16,17]. As another example, the novel  $LaH_{10}$  under high pressure can achieve superconductivity with the highest critical temperature among all superconducting materials synthesized so far [18]. Figure 1.2 shows the crystal structures of the materials mentioned above. These novel materials demonstrate the importance of high-pressure technology in searching for new materials.

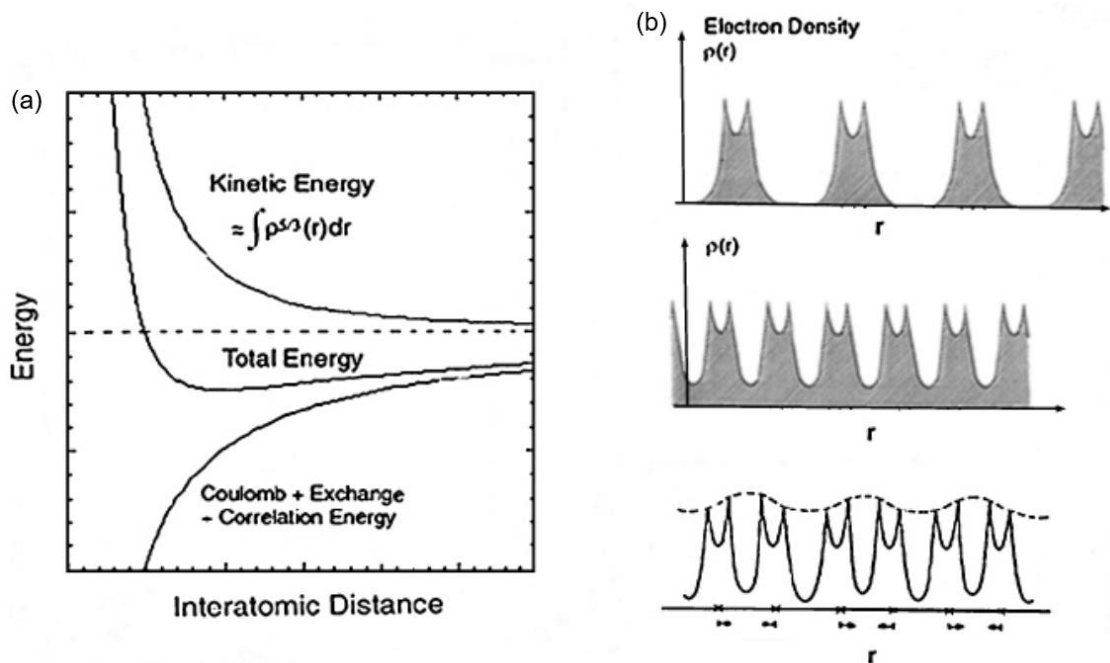


**Figure 1.1:** (a) The evolution of the total, electronic kinetic, and electronic potential energies with the interatomic distance [2]. (b) Building up electron density between atoms by shortening chemical bonds under compression [19].

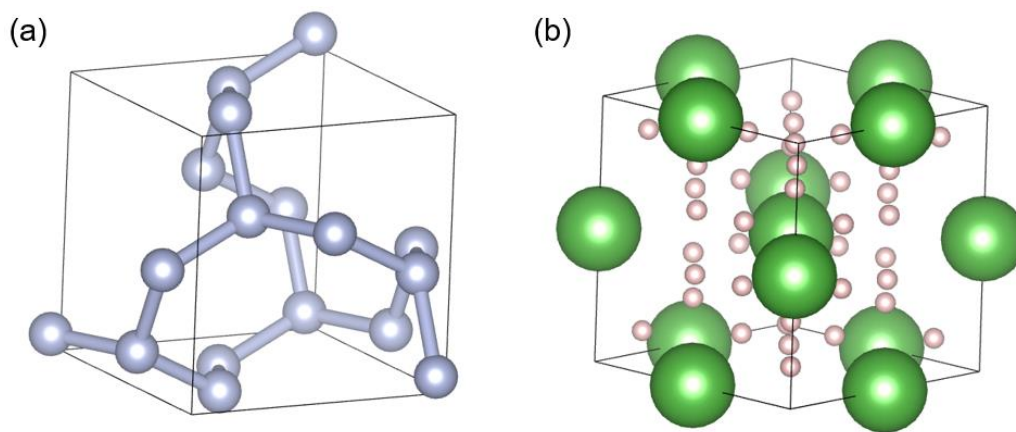


**Figure 1.2:** Novel materials discovered in high-pressure studies. (a) Polymeric nitrogen [16,17]. (b) Superconductor LaH<sub>10</sub> [18].

Technically, there are two ways to generate high-pressure conditions: dynamic and static. Dynamic compression is generated by shock waves, and can provide invaluable information about time-dependent transformations at pressures of up to a tera-pascal [20]. Currently, dynamic compression technologies are used to synthesize novel materials.

Static compression is generated by the diamond anvil cell (DAC), a device widely used for high-pressure experiments under laboratory conditions. DAC can generate high pressures up to 200 gigapascals (GPa), and possibly up to about 770 GPa [12,21–25]. Figure 1.3 shows the schematic of a symmetric DAC. In DAC experiments, a sample is loaded between the culets of two diamonds anvils and then sealed by gaskets. The ruby calibration is applied for accurate pressure measurements using the shift in ruby fluorescence. In order to control applied pressure, a force-generation device as one of the main components in the DAC apparatus is applied using either a lever arm or tightening screws. For an opposed diamond anvil device with small flat areas, the pressure  $P$  created in the DAC is given by the equation:

$$P = \frac{F}{S}, \quad (1.1)$$

where  $F$  is the applied force and  $S$  is the area of the diamond anvil. The principle of high pressure generated by the DAC is relevant to the typical culet sizes of diamond anvils, which are about 100–250 microns. Therefore, extremely high pressures can be obtained by applying a moderate force to a very small area.

To probe chemical and physical changes in materials at high pressures, advanced tools such as optical and vibrational spectroscopies (both IR and Raman spectra), x-ray and neutron scattering methods are commonly used [27–32]. However, these techniques rarely provide enough information to identify structural changes. By contrast, electronic structure calculations can predict crystal structures and dynamic changes under compression and may be applied to simulate pathways of pressure-induced phase transitions. In particular, density functional theory (DFT) calculations of materials under high pressures have enabled significant progress, ranging from structure determination and spectroscopic prediction to phase-transition diagrams [29,33–40]. An overview of the prevailing computational methods used in high-pressure materials research is provided in Section 1.3.

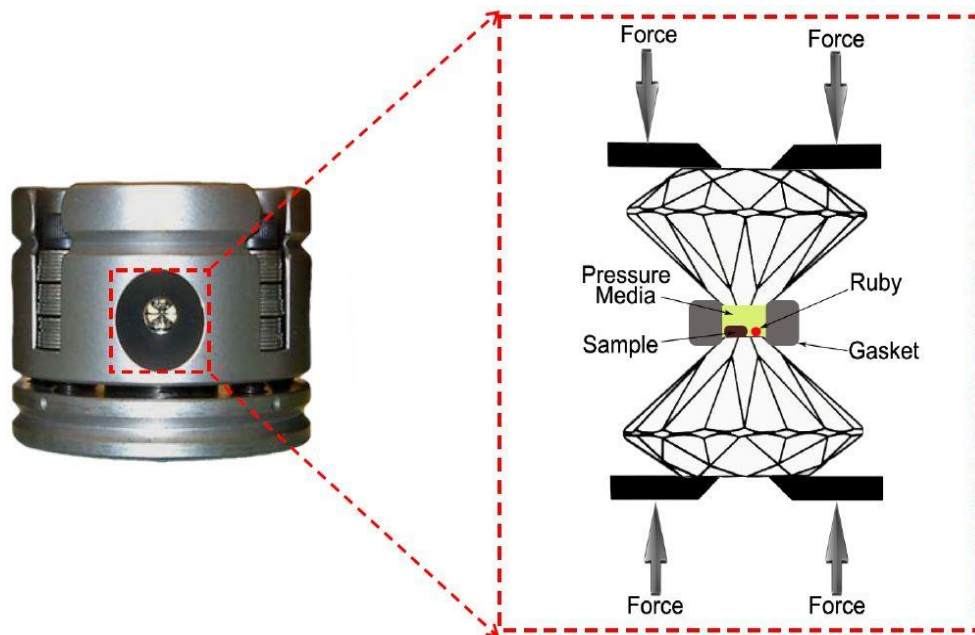
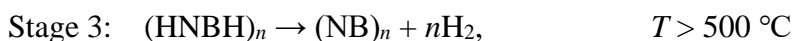


**Figure 1.3:** Photograph and enlarged schematic image of a DAC [26].

## 1.2 Hydrogen storage materials

Modern industrial production and transportation heavily rely on petroleum, natural gas, and coal. Unfortunately, consumption of these fuels releases into the atmosphere huge amounts of carbon dioxide, environmentally harmful carbon particulates, and nitrogen oxides. In this context, elemental hydrogen has long attracted considerable interest as a potential energy carrier due to its natural abundance and environmental friendliness [41–43]. Previously developed solid-state hydrogen storage materials with high gravimetric and volumetric hydrogen density are essential in the transportation and utilization of hydrogen [44].

Ammonia borane ( $\text{NH}_3\cdot\text{BH}_3$ ) has been considered as one of the particularly promising hydrogen storage materials because of its high hydrogen content (19.6% by mass) and stability under ambient conditions [45–49]. The production of elemental hydrogen from ammonia borane is realized via the following sequential thermal dehydrogenation processes:



Due to its excellent properties as a hydrogen storage material,  $\text{NH}_3\cdot\text{BH}_3$  has attracted considerable attention of high-pressure scientists. Under ambient conditions, this compound adopts a tetragonal structure of  $I4mm$  symmetry [50]. Early spectroscopy studies suggested that  $\text{NH}_3\cdot\text{BH}_3$  undergoes two phase transitions upon compression to 4 GPa [51,52]. Later, Lin *et al.* [53] and Xie *et al.* [28] reported other new phase transformations of  $\text{NH}_3\cdot\text{BH}_3$  around 20 GPa using Raman spectroscopy and a combination of IR/Raman spectroscopy, respectively. With the implementation of X-ray diffraction and DFT calculations on  $\text{NH}_3\cdot\text{BH}_3$ , a new orthorhombic structure of  $Cmc2_1$  symmetry was established at pressures above 1.5 GPa [54,55] and another new triclinic structure of  $P1$  symmetry was proposed at 8 GPa [56]. Using *in situ* low-temperature

Raman spectroscopy, Liu and Song extended the phase diagram of  $\text{NH}_3 \cdot \text{BH}_3$  from 0 to 15 GPa in the temperature range of 80 to 350 K [57]. Almost at the same time, a new phase of  $\text{NH}_3 \cdot \text{BH}_3$  of  $P2_1$  symmetry at 12.9 GPa was reported by using X-ray diffraction and DFT calculations [27]. More recently, a new phase transition of  $\text{NH}_3 \cdot \text{BH}_3$  was observed at 27 GPa using high-pressure Raman spectroscopy study up to 65 GPa [58]. All these high-pressure studies on  $\text{NH}_3 \cdot \text{BH}_3$  have been helpful for developing improved hydrogen storage materials.

In order to understand the nature of phase transitions of hydrogen storage materials at high pressures, theoretical calculations are usually applied to predict new phases and give insights into how stored hydrogen can be released at appropriate conditions. As an example, two different decomposition pathways of  $\text{NH}_3 \cdot \text{BH}_3$  were proposed by John *et al.* [59] using DFT calculations at atmospheric pressure and 6 GPa. In addition, computational studies on  $\text{NH}_3 \cdot \text{BH}_3$  proved that the N-H...H-B interaction plays an important role in phase transitions and can facilitate the release of molecular  $\text{H}_2$  from solid structures [27,60]. More examples of computational studies on hydrogen storage materials are listed in Table 1.1; the methodologies chosen to implement the DFT calculations will be discussed in more detail in Section 1.3.

Practical application of  $\text{NH}_3 \cdot \text{BH}_3$  as a hydrogen storage material faces multiple technological challenges including slow decomposition kinetics, relatively high initial temperature of the reactions, and harmful by-products (ammonia or borazine) that damage the fuel cell. Therefore, significant effort has been made to address these issues through the use of nanoscaffolds, base-metal catalysis, ionic liquids, doping, and structural modification of  $\text{NH}_3 \cdot \text{BH}_3$  derivatives. For instance, substituting one or more hydrogen atoms in  $\text{NH}_3 \cdot \text{BH}_3$  by organic groups or metal ions leads to various new compounds such as methylamine-borane ( $\text{Me}_n\text{H}_{3-n}\text{N} \cdot \text{BH}_3$  ( $n = 1-3$ )), sodium amidoborane ( $\text{NaNH}_2\text{BH}_3$ ), and bimetallic amidoborane ( $\text{Na}[\text{Li}(\text{NH}_2\text{BH}_3)_2]$ ) [61–71]. These derivatives of  $\text{NH}_3\text{BH}_3$  show significantly enhanced dehydrogenation performance relative to  $\text{NH}_3 \cdot \text{BH}_3$ .



**Table 1.1:** Computational studies of hydrogen storage materials at high pressures.

<b>Material</b>	<b>Pressure range</b>	<b>DFT functional</b>	<b>Computational packages</b>	<b>Major Findings</b>	<b>Reference</b>
Diborane (B <sub>2</sub> H <sub>6</sub> )	0–200 GPa	LDA, PBEsol, HSE06	Quantum Espresso, USPEX	New high-pressure phases, superconductivity, and simulated Raman spectra	[29,39]
Ammonia borane (NH <sub>3</sub> BH <sub>3</sub> )	0–40 GPa	vdW-DF, PBE, LDA	Quantum Espresso and VASP	New high-pressure phases, evolutionary investigation of dihydrogen bonds, simulated X-ray diffraction patterns, H <sub>2</sub> formation in NH <sub>3</sub> ·BH <sub>3</sub>	[27,59,60]
Lithiumamido-borane (LiNH <sub>2</sub> BH <sub>3</sub> )	0–100 GPa	PW91	VASP	New high-pressure phases	[32]
Lithium amide (LiNH <sub>2</sub> )	0–25 GPa	PBEsol	CASTEP	New high-pressure phases	[72]
CaH <sub>4</sub>	0–116 GPa	PBE	VASP	New high-pressure phases and simulated Raman spectra	[73]
LaH <sub>10</sub>	0–230 GPa	PBE	Quantum Espresso, VASP	New high-pressure phases, superconductivity	[74]

An essential feature of  $\text{NH}_3\cdot\text{BH}_3$  and its derivatives relevant to their ability to store and release hydrogen is the presence of so-called dihydrogen bonds. As is well known, the conventional hydrogen bond is formed by a proton donor (X) and an atom with a lone electron pair (Y) in the form of  $\text{X-H}\cdots\text{Y}$ . Similarly, most of  $\text{NH}_3\cdot\text{BH}_3$  and its derivatives with protonic N-H and hydridic B-H groups can form dihydrogen bonds  $\text{N-H}^{\delta+}\cdots\delta^-\text{H-B}$  via charge-transfer interaction. This requires that the intermolecular  $\text{H}\cdots\text{H}$  distance be shorter than the sum of the van der Waals (vdW) radii, typically in the range of 1.7–2.2 Å [75]. Figure 1.4 shows the N-H...H-B framework between two  $\text{NH}_3\text{BH}_3$  molecules. The hydrogen release in the dehydrogenation process of  $\text{NH}_3\cdot\text{BH}_3$  is believed to initially undergo an induction process, where the dihydrogen network of  $\text{NH}_3\cdot\text{BH}_3$  is disrupted to promote hydrogen release through dehydrocoupling [76]. Using electronic structure calculations, Patwari [77] suggested that dihydrogen bonding plays an important role in  $\text{H}_2$  elimination from  $\text{NH}_3\cdot\text{BH}_3$  network via  $\eta^2\text{-H}_2$  complex as an intermediate. In this thesis, the evolution of N-H...H-B frameworks will be discussed in Chapter 5.

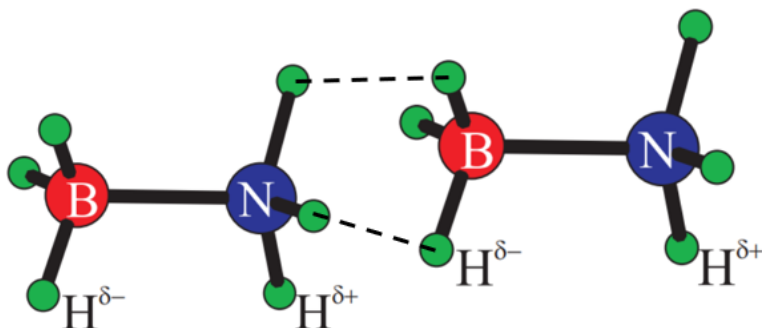


**Figure 1.4:** The dihydrogen bonding framework (N-H...H-B) between  $\text{NH}_3\text{BH}_3$  molecules [67].

### 1.3 Overview of computational methods for materials at high pressures

In general, there are two types of theoretical simulation techniques for studying materials at high pressures. Techniques of the first type, used for static and dynamic calculations of pressure-induced structural changes, include DFT, quantum Monte-Carlo, and molecular dynamics. Techniques of the second type, concerned with structure search, include simulated annealing,

random sampling, generic algorithms, and swarm optimization algorithms [12]. Most techniques of both types rely on DFT calculations to provide total energies and enthalpies of the system. Moreover, DFT calculations implemented for condensed-matter physics are also used for simulating electronic band structures as well as vibrational and nuclear magnetic resonance (NMR) spectra. The theoretical principles of DFT will be discussed in Chapter 2.

Examples of software packages widely used for static and dynamic calculations include: Quantum Espresso [78], VASP (Vienna *Ab Initio* Simulation Package) [79], CASTEP (Cambridge Serial Total Energy Package) [80], CPMD (Car–Parrinello Molecular Dynamics) [81], CRYSTAL [82], CP2K [83] and SIESTA (Spanish Initiative for Electronic Simulations with Thousands of Atoms) [84]. All of them have the capability to perform molecular dynamic simulations and calculate thermodynamic structure changes under compression. Moreover, Quantum Espresso, VASP, CASTEP, CRYSTAL, and CP2K can also be applied to simulate IR and Raman spectra of condensed phases. CASTEP and CRYSTAL can also perform solid-state NMR calculations.

Over the past decade, several simulation packages have been developed and used to predict crystal structures of materials at high pressures [29,85–87]. For instance, the AIRSS (*Ab Initio* Random Structure Searching) [88] package was developed by using stochastic sampling of configuration space with the possibility to use symmetry, chemical, and physical constraints. Now it is widely used to simulate crystals, low-dimensional materials, and clusters. The CALYPSO (Crystal Structure Analysis by Particle Swarm Optimization) package [89] performs particle swarm optimizations for crystal structure analysis and has been used to predict superconducting, super-hard and energetic materials. Another popular package is the XtalOpt (Evolutionary Crystal Structure Prediction) [90]. Finally, the USPEX (Universal Structure Predictor: Evolutionary Xtallography) [91,92] package developed by Oganov and co-workers, offers several methods including evolutionary search, random sampling, evolutionary meta-dynamics, and transition path sampling. The USPEX package has been successful in the efficient and accurate prediction of molecular crystals for studies of materials under high-pressures, such as novel high-pressure phases of  $\text{NaCl}_3$ ,  $\text{Mg}_3\text{O}_2$ ,  $\text{Mg}(\text{BH}_4)_2$ ,  $\text{MgSiO}_3$ , and  $\text{Al}_2\text{O}_3$  systems [93–97].

In this thesis, we employed Quantum Espresso and USPEX, details of which are provided in Chapter 2. Table 1.2 summarizes all the computational methods mentioned here.

**Table 1.2:** Computational packages applied to high-pressure materials science.

<b>Electronic structure computation</b>	<b>Basis set</b>	<b>Pseudopotentials</b>	<b>License</b>	<b>Open source software</b>	<b>Examples of study</b>
Quantum Espresso	Plane-wave	Norm-conserving and ultrasoft	Free	Yes	High-pressure studies in ammonia borane [27] and diborane [29,39,40]
VASP	Plane-wave	Ultrasoft	Academic, commercial	Yes	High-pressure phase determinations in $\text{LiNH}_2\text{BH}_3$ and $\text{NaNH}_2\text{BH}_3$ [33,34]
CASTEP	Plane-wave	Norm-conserving	Academic, commercial	Yes	Investigation of the structural and mechanical properties of type-VIII $\text{Ba}_8\text{Si}_{46}$ clathrate [98]
CPMD	Plane-wave	Goedecker–Teter–Hutter-type and norm-conserving	Academic	Yes	Investigations of quantum nuclear dynamics of protons within layered hydroxides [99]
CRYSTAL	Gaussian	All-electron Gaussian	Academic, commercial	No	Structure and thermodynamic properties investigations in $\text{NaMgH}_3$ perovskite [100]
CP2K	Gaussian and plane-wave	All-electron Goedecker–Teter–Hutter-type and Gaussian	Free	Yes	Periodic continuum solvation model integrated with first-principles calculations for solid surfaces [101]

SIESTA	Numerical atomic orbitals	Norm-conserving	Free	Yes	High-pressure studies in PbTe [102] and semiconducting germaniums [103]
<b>Crystal structure prediction</b>	<b>Algorithms</b>	<b>Electronic structure packages</b>	<b>License</b>	<b>Open source code</b>	<b>Examples of study</b>
USPEX	Evolutionary algorithms, random sampling, evolutionary meta-dynamics, and transition path sampling	Quantum Espresso, VASP, CASTEP, CP2K, and SIESTA	Academic, commercial	Yes	High-pressure phase predictions of diborane [29], ZnCO <sub>3</sub> [104], Fe <sub>7</sub> N <sub>3</sub> and Fe <sub>7</sub> C <sub>3</sub> [105]
AIRSS	Stochastic sampling of configuration space	VASP and CASTEP	Free	Yes	High-pressure phase predictions of Arsenic [106], Fe <sub>7</sub> N <sub>3</sub> and Fe <sub>7</sub> C <sub>3</sub> [105]
CALYPSO	Particle swarm optimization	Quantum Espresso, VASP, and CASTEP	Academic, commercial	Yes	High-pressure phase predictions of Weyl semimetal NbAs and NbP [107]
XtalOpt	Evolutionary algorithms	Quantum Espresso, VASP, CASTEP, and SIESTA	Free	Yes	Crystal structure prediction in super-hard materials [108]

## 1.4 Scope of this study

As stated above, ammonia borane has a large number of derivatives. In this thesis, we focused on one particular derivative of  $\text{NH}_3\cdot\text{BH}_3$  named ethylenediamine bisborane (EDAB),  $\text{BH}_3\cdot\text{NH}_2\text{CH}_2\text{CH}_2\text{NH}_2\cdot\text{BH}_3$  (space group: *Pbca*). Figure 1.5 shows a unit cell of EDAB under ambient pressure [109]. EDAB is more stable than  $\text{NH}_3\cdot\text{BH}_3$  at temperatures below 100 °C and releases ca. 10 wt% of molecular hydrogen between 100–200 °C at ambient pressure, without detectable impurities [44,109–112]. Neiner *et al.* [113] showed that the rate of hydrogen release of EDAB is faster than that of  $\text{NH}_3\cdot\text{BH}_3$  at temperatures above 120 °C. These properties make EDAB a promising candidate for a hydrogen storage material.

In order to investigate the phase transitions of EDAB under high pressures, Wang *et al.* [114] applied a combination of *in situ* Fourier-transform infrared (IR) spectroscopy, Raman spectroscopy and synchrotron XRD techniques. The changes in spectroscopies and X-ray diffraction suggested two phase transitions at around 1.0 and 8.0 GPa in a pressure range of 0–17 GPa, as shown in Figure 1.6 [114]. In this study, we employ Kohn–Sham DFT calculations to identify the experimentally suggested phase transitions of EDAB and to determine crystal structures of these new phases. We also investigate the evolution of dihydrogen bonding frameworks in EDAB upon compression and report new insights into these phase transitions. Our computational results reveal new polymorphs of EDAB where the transformation mechanism can be analyzed using structural information. These findings contribute to the fundamental understanding of the structure-property relationship, which is helpful for the development of aminoborane-based hydrogen storage materials.

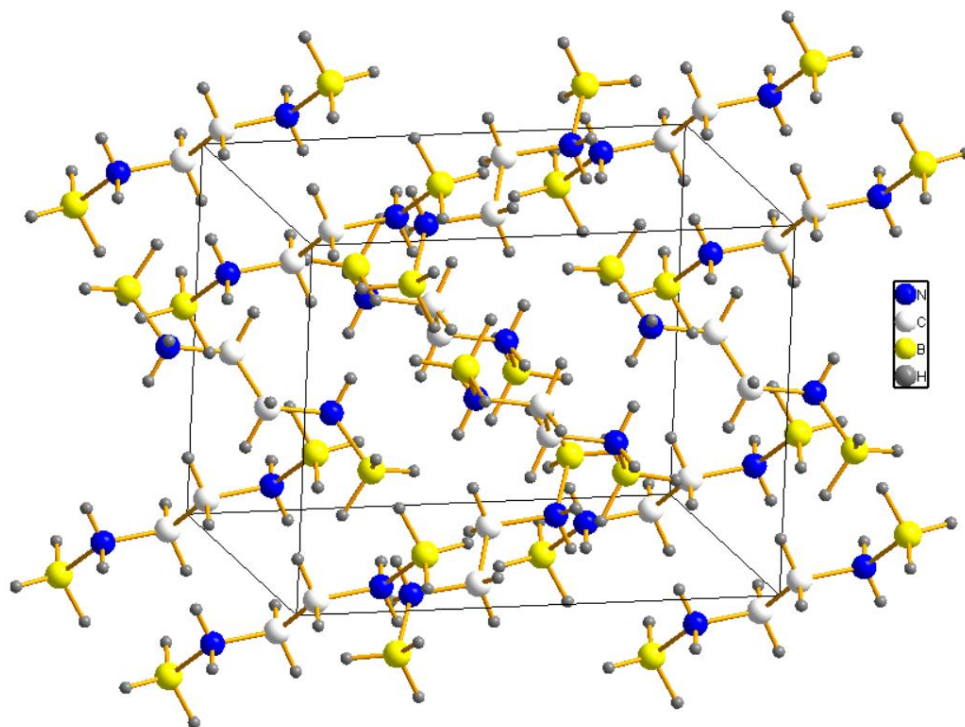


**Figure 1.5:** The unit cell of EDAB (space group: *Pbca*,  $a = 10.761 \text{ \AA}$ ,  $b = 8.172 \text{ \AA}$ ,  $c = 8.131 \text{ \AA}$ ) at ambient pressure. There are four molecules per unit cell [109].

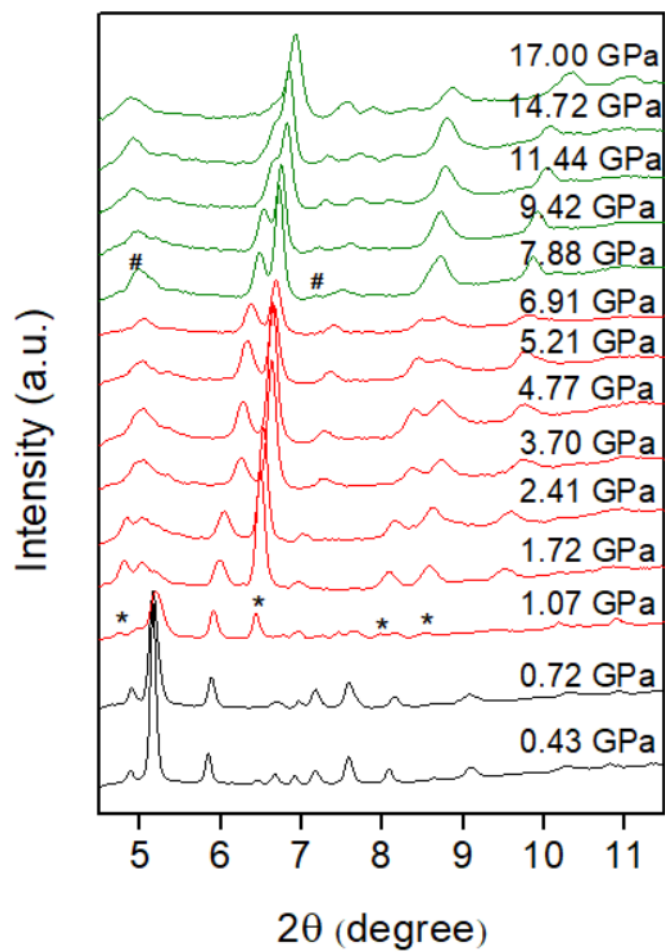


**Figure 1.6:** Synchrotron XRD patterns of EDAB under compression at room temperature, \* and # mark the appearance of new peaks in phase II and phase III [114].



## 2 Computational methodology

### 2.1 Kohn–Sham density functional theory

The Kohn–Sham [115,116] density functional theory (DFT) is a quantum-mechanical method for exploring the electronic structure of many-electron systems (atoms, molecules and solids). In this theory, electronic properties are determined by using an energy functional of the ground-state electron density,  $\rho(\mathbf{r})$ . The central part of the Kohn–Sham DFT is the one-electron Schrödinger equation for a fictitious system of non-interacting electrons with the same ground-state density as that of the system of interacting electrons. The Kohn–Sham wave function is a single Slater determinant constructed from a set of orbitals that are the lowest-energy solutions to the following equation:

$$\left[ -\frac{1}{2}\nabla^2 + v_{\text{eff}}(\mathbf{r}) \right] \phi_i(\mathbf{r}) = \varepsilon_i \phi_i(\mathbf{r}). \quad (2.1)$$

This is an eigenvalue equation in which  $\varepsilon_i$  is the energy of the Kohn–Sham orbital  $\phi_i$  and  $\rho(\mathbf{r})$  is given by:

$$\rho(\mathbf{r}) = \sum_{i=1}^{\text{occ.}} |\phi_i(\mathbf{r})|^2. \quad (2.2)$$

The total energy functional in the Kohn–Sham DFT has the form:

$$E[\rho] = T_s[\rho] + J[\rho] + E_{\text{xc}}[\rho] + \int v_{\text{ext}}(\mathbf{r})\rho(\mathbf{r})d\mathbf{r}, \quad (2.3)$$

where  $T_s[\rho]$  is the total kinetic energy of non-interacting electrons, given by:

$$T_s[\rho] = -\frac{1}{2} \sum_{i=1}^{\text{occ.}} \int \phi_i(\mathbf{r}) \nabla^2 \phi_i(\mathbf{r}) d\mathbf{r}, \quad (2.4)$$

and  $J[\rho]$  is the energy of the Coulomb self-repulsion of the electron density  $\rho$ :

$$J[\rho] = \frac{1}{2} \iint d\mathbf{r}d\mathbf{r}' \frac{\rho(\mathbf{r})\rho(\mathbf{r}')}{|\mathbf{r}-\mathbf{r}'|}. \quad (2.5)$$

In Eq. (2.3),  $E_{xc}[\rho]$  is the exchange-correlation energy functional. Variation of the total energy functional with respect to a set of Kohn–Sham orbitals  $\phi_i$  under appropriate constraints [117] yields the Kohn–Sham potential, given as:

$$v_{eff}(\mathbf{r}) = v_{ext}(\mathbf{r}) + \int \frac{\rho(\mathbf{r}')}{|\mathbf{r}-\mathbf{r}'|} d\mathbf{r}' + \frac{\delta E_{xc}[\rho]}{\delta \rho(\mathbf{r})}, \quad (2.6)$$

where the  $\frac{\delta E_{xc}[\rho]}{\delta \rho(\mathbf{r})}$  is the exchange-correlation potential. The exchange-correlation potential and the corresponding energy functionals are unknown. Thus, approximate density functionals have been developed and will be briefly discussed in the following sections.

### 2.1.1 LDA functional

In the local density approximation (LDA) [118], the exchange-correlation energy density depends only on  $\rho(\mathbf{r})$  at each point in space. The exchange-correlation energy of the LDA type is given by:

$$E_{xc}^{LDA}[\rho] = \int \varepsilon_{xc}(\rho) \rho(\mathbf{r}) d\mathbf{r}. \quad (2.7)$$

The LDA for the exchange energy of a homogenous electron gas is known analytically:

$$E_x^{LDA}[\rho] = -\frac{3}{4} \left( \frac{3}{\pi} \right)^{\frac{1}{3}} \int \rho(\mathbf{r})^{\frac{4}{3}} d\mathbf{r}. \quad (2.8)$$

There are several available analytical expressions for the correlation energy  $E_c^{LDA}[\rho]$  of the homogenous electron gas interpolating between the known exact high- and low-density limits. Using different analytical forms for the correlation energy per electron,  $\varepsilon_c(\rho)$ , various approaches lead to several LDA parametrizations of the correlation functional, including Vosko–Wilk–Nusair (VWN) [119], Perdew–Zunger (PZ81) [120], Cole–Perdew (CP) [121] and Perdew–Wang (PW92) [122].

## 2.1.2 PBE functional

It is known that the LDA tends to underestimate the exchange energy and overestimate the correlation energy [123]. To deal with this limitation, approximations in terms of the gradient of the density to account the non-homogeneity of the true electron density have been proposed. These functionals are referred to as generalized-gradient approximations (GGA) [124]. The exchange-correlation energy of a GGA type is given by:

$$E_{\text{XC}}^{\text{GGA}}[\rho] = \int \varepsilon_{\text{XC}}(\rho, \nabla\rho) \rho(\mathbf{r}) d\mathbf{r}, \quad (2.9)$$

where  $\varepsilon_{\text{XC}}(\rho, \nabla\rho)$  is the exchange-correlation energy per electron.

In general, GGA can reliably reproduce experimental molecular structures and ground-state energy. For our studies on high-pressures induced structural transformations, we have employed two GGAs: the Perdew–Burke–Ernzerhof (PBE) functional [125] and its modification for solids (PBEsol) [126].

Any approximate exchange functional should reduce to Eq. (2.8) when the electron density becomes constant. Deviations from homogeneity are described with the exchange-enhancement factor [127]. This factor is  $F_x \leq 1.804$ . Applying these conditions, Perdew, Burke, and Ernzerhof proposed a non-empirical exchange-correlation functional with the PBE exchange part of the form:

$$E_{\text{X}}^{\text{PBE}} = -\frac{3}{4} \left( \frac{3}{\pi} \right)^{\frac{1}{3}} \int \rho(\mathbf{r})^{\frac{4}{3}} F_x(s) d\mathbf{r}. \quad (2.10)$$

The PBE enhancement factor is:

$$F_{\text{X}}^{\text{PBE}}(s) = 1 + \frac{\mu s^2}{1 + \frac{\mu s^2}{k}}, \quad (2.11)$$

where  $k = 0.0804$  and  $\mu = 0.21951$  is a parameter determined by the condition that the second-order gradient coefficient for the exchange contribution cancel the corresponding counterpart for the correlation contribution. This value ensures that the PBE exchange-correlation can reach LDA

in the slowly varying density regions. The correlation part of the PBE functional has a more complicated expression which may be found in Ref. [125].

### 2.1.3 PBEsol functional

Due to its non-empirical and relatively simple form, the PBE functional has become the workhorse for computational condensed-matter studies. It is also known that PBE can overestimate bond lengths as well as lattice parameters by 1 %. Therefore, its revision, PBEsol, has been developed by Perdew *et al.* in 2008 [126]. PBEsol differs from PBE in that it uses the value  $\mu = 10/81 \approx 0.12346$ , which is about half as large as  $\mu = 0.21951$  of the PBE functional. PBEsol has been demonstrated to give more accurate results for solids than PBE [125]. For this reason, we also employed the PBEsol functional to study crystal structures at high pressures [128].

### 2.1.4 Van der Waals density functional

The van der Waals force is a distance-dependent interaction between atoms or molecules. It is different from the interactions responsible for the formation of ionic or covalent bonds because the van der Waals (vdW) forces vanish more quickly with distance between interacting molecules. At ambient or lower pressures, van der Waals forces can play a key role in molecular crystals. Thus, the van der Waals density functional (vdW-DF) [129] has been developed to account for noncovalent interactions in electronic structure calculations.

In vdW-DF, the functional energy is defined as:

$$E = E_X^{\text{GGA}} + E_C^{\text{LDA}} + E_C^{\text{NL}}, \quad (2.12)$$

where  $E_C^{\text{NL}}$  is a nonlocal functional. In the Quantum ESPRESSO package, nonlocal functionals called vdW-DF1 and vdW-DF2 have been implemented. The development of these functionals involves physical principles such as the local field response function and irreducible correlation

function. The functional derivative of the nonlocal energy functional  $E_C^{NL}$  for the corresponding potential is straightforward [130,131].

## 2.2 Periodic structures and plane waves

Unlike atoms and molecules, crystal structures are usually represented as infinite periodic systems. For Kohn–Sham DFT calculations of periodic systems, Bloch waves are normally used, which have the following form:

$$\varphi_{\mathbf{k}}(\mathbf{r}) = \exp(i\mathbf{k} \cdot \mathbf{r})u_{\mathbf{k}}(\mathbf{r}), \quad (2.13)$$

where  $u_{\mathbf{k}}(\mathbf{r})$  is a periodic real-space function with the same periodicity as the crystal lattice. The functions  $\exp(i\mathbf{k} \cdot \mathbf{r})$  are called plane waves. Eq. (2.13) expresses a result known as Bloch’s theorem. It means that if the potential has some periodicity, the corresponding wave function has the same periodicity. The space of  $\mathbf{r}$  vectors is called real space, and the space of  $\mathbf{k}$  vectors is called reciprocal space (or  $\mathbf{k}$  space). In fact,  $\mathbf{k}$  is the Bloch wave vector. The basis vectors of the real space and the reciprocal space are related by:

$$\mathbf{b}_1 = 2\pi \frac{\mathbf{a}_2 \times \mathbf{a}_3}{\mathbf{a}_1 \cdot (\mathbf{a}_2 \times \mathbf{a}_3)}, \quad \mathbf{b}_2 = 2\pi \frac{\mathbf{a}_3 \times \mathbf{a}_1}{\mathbf{a}_2 \cdot (\mathbf{a}_3 \times \mathbf{a}_1)}, \quad \mathbf{b}_3 = 2\pi \frac{\mathbf{a}_1 \times \mathbf{a}_2}{\mathbf{a}_3 \cdot (\mathbf{a}_1 \times \mathbf{a}_2)}, \quad (2.14)$$

where  $\mathbf{a}_i$  are the lattice vectors defining positions in real space, while  $\mathbf{b}_i$  are the reciprocal-lattice vectors.

## 2.3 $\mathbf{k}$ -point mesh in Brillouin zone

The primitive cell in the reciprocal space is known as the first Brillouin zone. In Kohn-Sham DFT calculations on periodic systems, integrations of various physical quantities within the Brillouin zone can be replaced by the numerical summation over a finite  $\mathbf{k}$ -point mesh. It can be calculated by the following equation with a  $\mathbf{k}$ -point mesh,

$$\int f(x)dx \approx \sum_{j=1}^n c_j f(x_j), \quad (2.15)$$

where  $c_j$  is a numerical weight. In this work, we employed the Monkhorst-Pack scheme [132] for the  $\mathbf{k}$ -point mesh selection. In the Monkhorst-Pack scheme,  $\mathbf{k}$  points are uniformly distributed within the primitive unit cell according to

$$\mathbf{k} = u_1 \mathbf{b}_1 + u_2 \mathbf{b}_2 + u_3 \mathbf{b}_3, \quad (2.16)$$

where  $\mathbf{b}_i$  are the reciprocal lattice vectors, and

$$u_i = \frac{2m - M_i - 1}{2M_i}, \quad m = 1, 2, 3, \dots, M_i; \text{ and } i = 1, 2, 3. \quad (2.17)$$

The general form of this mesh is  $M_1 \times M_2 \times M_3$ .

## 2.4 Kinetic energy cutoff

In Eq. (2.13), the function  $u_{\mathbf{k}}(\mathbf{r})$  is periodic in space and can be expanded in terms of a special set of plane waves:

$$u_{\mathbf{k}}(\mathbf{r}) = \sum_{\mathbf{G}} c_{\mathbf{G}} \exp(i\mathbf{G} \cdot \mathbf{r}), \quad (2.18)$$

where the summation is over all vectors defined by  $\mathbf{G} = m_1 \mathbf{b}_1 + m_2 \mathbf{b}_2 + m_3 \mathbf{b}_3$  with integer values for  $m_j$ . For any real-space lattice vector  $\mathbf{a}_j$ ,  $\mathbf{G} \cdot \mathbf{a}_j = 2\pi m_j$ . Substituting Eq. (2.18) to Eq. (2.13) gives:

$$\varphi_{\mathbf{k}}(\mathbf{r}) = \sum_{\mathbf{G}+\mathbf{k}} c_{\mathbf{k}+\mathbf{G}} \exp[i(\mathbf{k} + \mathbf{G}) \cdot \mathbf{r}]. \quad (2.19)$$

This infinite summation can be truncated to include only solutions with a kinetic energy less than a predetermined value:

$$E_{\text{cut}} = \frac{G_{\text{cut}}^2}{2}. \quad (2.20)$$

The infinite sum then reduces to:

$$\varphi_{\mathbf{k}}(\mathbf{r}) = \sum_{|\mathbf{k}+\mathbf{G}| < G_{\text{cut}}} c_{\mathbf{k}+\mathbf{G}} \exp[i(\mathbf{k} + \mathbf{G}) \cdot \mathbf{r}]. \quad (2.21)$$

In general, the accuracy of calculations on periodic systems can always be systematically improved by increasing the kinetic energy cutoff, which necessarily entails a higher computational cost. Therefore, it is crucial to test convergence of the total energy at the very beginning in order to keep a balance between computational cost and accuracy.

## 2.5 Pseudopotentials

Usually, core electrons are not important in defining chemical bonding and physical properties of materials. In practical calculations on periodic systems, core electrons are often replaced by pseudopotentials. A pseudopotential replaces the core electrons with a smoothed potential function chosen to match various important physical and mathematical properties of the true ion core. Hydrogen is a special atom with valence electron and no core electrons. However, the pseudopotential for hydrogen atom is also used to smooth out the electron density near hydrogen nuclei and thereby significantly reduce the number of plane waves required. One of the most widely used methods of defining a pseudopotential is due to Vanderbilt [133]. Vanderbilt pseudopotentials are also known as ultrasoft pseudopotentials (USPPs).

The construction of pseudopotentials requires orbitals of core and valence electrons to be mutually orthogonal. Such orbitals are obtained by diagonalizing a Hermitian operator constructed with eigenstates from all-electron calculations. There are several packages available for the generation of pseudopotentials. Figure 2.1 shows the pseudopotentials generated for carbon with the PBE functional using the OPIUM package [134]. The parameters are taken from the pseudopotential library [78] of the Quantum ESPRESSO package.

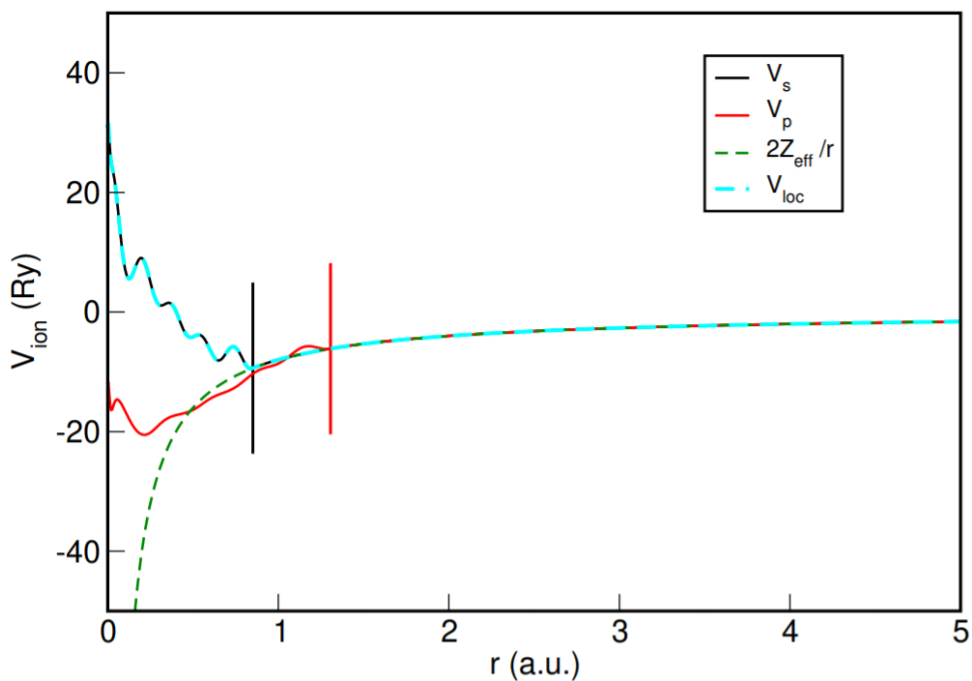


**Figure 2.1:** The norm-conserving pseudopotential of carbon.

Figure 2.1 shows that the pseudopotentials are approximately converged to the effective Coulomb potential beyond the cutoff radii, 0.84 Å for the 2s electrons and 1.29 Å for the 2p electrons. The selection of the cutoff radii can affect the calculation results. The library from the Quantum ESPRESSO package provides optimized cutoff radii. Figure 2.2 shows the wave functions of carbon. Again, beyond the cutoff radius, the pseudo-wave functions are exactly equal to the all-electron wave functions.



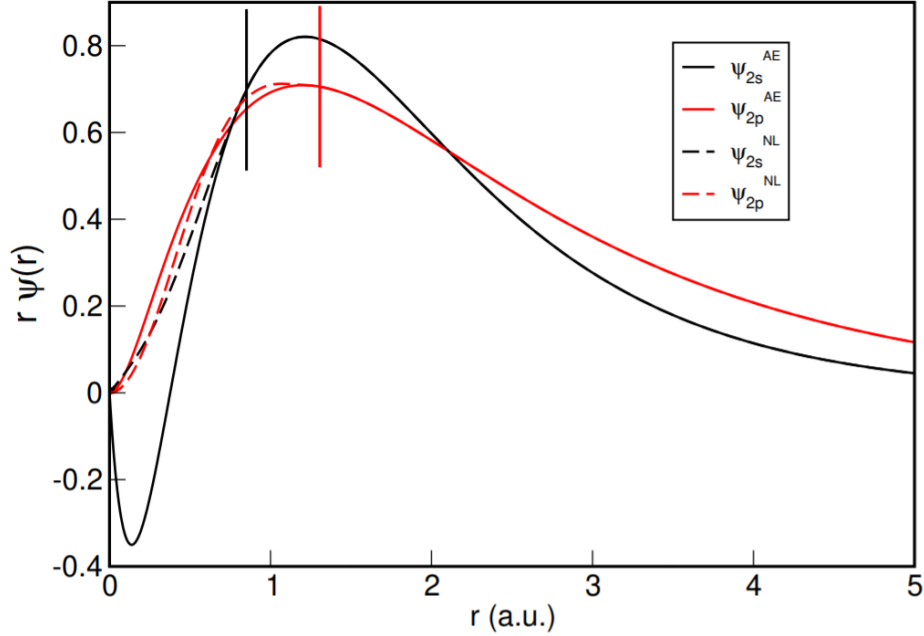


**Figure 2.2:** All electron and pseudopotential wave functions. “AE” stands for all-electron while “NL” is non-local pseudopotential.

## 2.6 Evolutionary prediction of high-pressure structures

We used the DICVOL [135] program to estimate possible cell parameters of new high-pressure phases of EDAB based on the experimental XRD data. DICVOL is an indexing program for XRD pattern analysis on crystal lattices. The determination of lattice parameters is based on the XRD peak positions and intensities following the Bragg’s law,  $n\lambda = 2d\sin\theta$  ( $n$  is a positive integer,  $\lambda$  is the wavelength of the incident wave, and  $d$  is the spacing between crystal planes).

In order to generate plausible candidates with atomic positions and space groups based on the lattice parameters obtained by DICVOL, we employed the USPEX code developed by Oganov *et al.* [91,92]. This package combines first-principles enthalpy calculations with an evolutionary search algorithm. The algorithm incorporates “learning from the last generation”, which means that the structures of the offspring are similar to those of the more successful previous sampling structures. During this process, structures with the lowest enthalpies are selected to become parents of the new generation, and the process is repeated over multiple generations until a certain number

of suitable offsprings are generated. To ensure that good genes can be passed down from one generation to another, four variation operators are employed in the algorithm, including heredity, lattice mutation, permutation and special coordinate mutations. The heredity operator is used to generate child structures from combinations of random slices of two parent unit cells. Through lattice mutation, the shape of the unit cell can be applied with large random deformation. The permutation operator is employed to exchange chemical identities in pairs of atoms with different chemical properties. The special coordinate mutations are used for the displacements of the atoms. Thus, USPEX can predict the stable and metastable structures based only on the chemical composition, and it is a particularly useful tool in applications to high-pressure chemistry.

## 2.7 Summary of the optimized methodology for crystal-structure calculations

All plane-wave calculations were performed using the Quantum ESPRESSO package (version 6.3). Both lattice parameters and atomic positions for the reference structure and candidate structures of EDAB were optimized at a target pressure using enthalpy-minimizing calculations. The energy threshold for the convergence of Kohn–Sham self-consistent-field cycles was set to  $10^{-8}$  Ry. The Broyden–Fletcher–Goldfarb–Shanno quasi-Newton algorithm was applied to the lattice structure optimization with a  $10^{-4}$  Ry/Å threshold for the Hellmann–Feynman forces and  $5 \times 10^{-5}$  Ry for the total energy. All the calculations correspond to  $T = 0$  K.

### 2.7.1 Convergence testing calculations

To keep a balance between computational cost and accuracy, it is crucial to select appropriate cutoff energy and  $\mathbf{k}$ -point mesh when performing a Kohn–Sham DFT calculation using plane-wave basis functions. The initial crystal structure of EDAB used for all geometry optimizations was taken from the experiment under ambient conditions [109]. Figure 2.3 shows the results of structural optimization calculations of EDAB with different kinetic energy cutoff and  $\mathbf{k}$ -point mesh. We used the PBE functional with ultrasoft pseudopotentials for all these calculations. It shows that the total energy of EDAB per unit cell is converged to  $-5170.766$  eV.

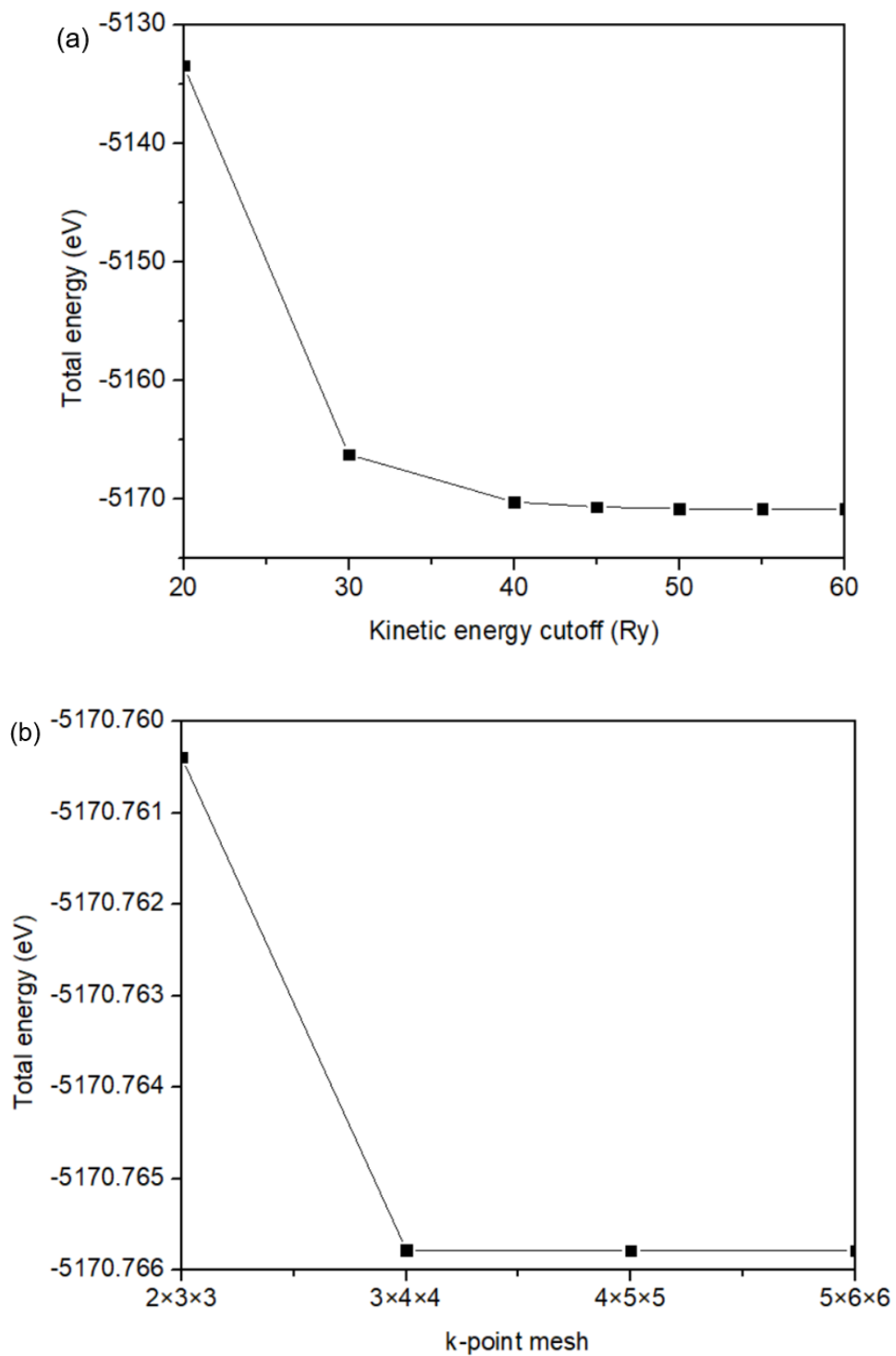


**Figure 2.3:** The structure optimization calculations of EDAB were performed by using the PBE functional and ultrasoft pseudopotentials under ambient pressure. (a) Total energy versus kinetic energy cutoff. (b) Total energy versus  $\mathbf{k}$ -point mesh.

## 2.7.2 Selection of density functionals

In order to select an appropriate functional for further calculations, we compared the optimized structures obtained using different functionals with the experimental lattice parameters. There are four functionals selected for these test calculations: LDA, PBE, PBEsol and vdW-DF. Our results are shown in Table 2.1. The LDA has the largest error among the four functionals. The calculations with PBEsol also show relatively large differences. The results of the vdW-DF and PBE functionals are significant improvements. The largest relative differences for the PBE and vdW-DF functionals are 1.7 % and 2.2 % in comparison with 3.9 % and 5.8 % for PBEsol and LDA functionals, respectively. Therefore, the vdW-DF and PBE functionals were chosen for further candidate structure calculations.

**Table 2.1:** Comparison of the lattice parameters of EDAB (space group: *Pbca*) optimized using four functionals with a 50 Ry kinetic energy cutoff and  $4 \times 5 \times 5$  **k**-point mesh under ambient pressure.

Functionals	Cell parameters and errors		
	<i>a</i>	<i>b</i>	<i>c</i>
Expt. (Å)	10.761	8.172	8.131
LDA (Å)	10.249	7.701	7.698
MARE (%)	4.8	5.8	5.3
PBEsol (Å)	10.687	7.849	7.922
MARE (%)	0.7	3.9	2.6
PBE (Å)	10.941	8.089	8.209
MARE (%)	1.7	1.0	1.0
vdW-DF (Å)	10.670	8.349	8.240
MARE (%)	0.8	2.2	1.3

\* MARE = mean absolute relative error

### 2.7.3 Selection of pseudopotentials

The pseudopotentials were taken from the Quantum ESPRESSO pseudopotential library [78]. We compared the ultrasoft (USPP) pseudopotentials against projector-augmented wave (PAW) pseudopotentials. As seen from Table 2.2, USPPs give slightly smaller mean absolute relative errors than PAW pseudopotentials. Therefore, USPPs were chosen for further candidate structure calculations.

**Table 2.2:** Comparison of the lattice parameters of EDAB (space group: *Pbca*) optimized using the USPP and PAW pseudopotentials with a 50 Ry kinetic energy cutoff and  $4\times 5\times 5$  **k**-point mesh under ambient pressure.

Pseudopotentials	Cell parameters and errors		
	<i>a</i>	<i>b</i>	<i>c</i>
Expt. (Å)	10.761	8.172	8.131
USPP (Å)	10.941	8.089	8.209
MARE (%)	1.67	1.01	0.96
PAW (Å)	10.943	8.090	8.210
MARE (%)	1.69	1.00	0.97

\* MARE = mean absolute relative error

## 3 Generation of candidate structures

### 3.1 Lattice parameter prediction at ambient pressures

After validating our computational settings, we employed the USPEX package to generate EDAB candidate structures of new phases. USPEX generates a very large number of structures which need to be screened by calculating enthalpies or XRD patterns. However, when dealing with unit cells containing a large number of atoms (as is the case with molecular crystals of EDAB), using USPEX to search candidates becomes too computationally expensive. This is due to the high number of possible lattice parameters or space groups possible for EDAB, and USPEX can generate thousands of unrealistic crystal structures. We narrowed down the list by analyzing the experimental XRD patterns using the DICVOL program and determining the possible lattice parameters for the crystal structure search.

The experimental XRD pattern shown in Figure 1.6 at 1.72 and 11.44 GPa were selected to estimate lattice parameters using DICVOL. Table 3.1 and 3.2 show the possible lattice parameters of new phases II and III generated using the DICVOL indexing software. There are 15 possible lattice parameters for phase II with all monoclinic symmetry, and 18 such parameters for phase III with monoclinic and orthorhombic symmetries. The determination of phase transition candidates requires further structure search simulations using USPEX.

**Table 3.1:** Possible lattice parameters of phase II generated according to the experimental XRD pattern at 1.72 GPa using DICVOL.

System	$a$ (Å)	$b$ (Å)	$c$ (Å)	$\alpha$ (°)	$\beta$ (°)	$\gamma$ (°)	$V$ (Å <sup>3</sup> )
Monoclinic	10.781	9.355	7.102	90.0	115.3	90.0	647
Monoclinic	10.060	9.355	7.102	90.0	104.4	90.0	647
Monoclinic	10.247	7.031	9.327	90.0	108.7	90.0	637
Monoclinic	8.325	10.482	8.092	90.0	103.2	90.0	687
Monoclinic	8.143	10.941	7.433	90.0	95.2	90.0	659
Monoclinic	8.152	11.015	7.330	90.0	95.5	90.0	655
Monoclinic	11.226	6.383	10.419	90.0	106.6	90.0	715
Monoclinic	11.365	6.445	10.628	90.0	106.6	90.0	722
Monoclinic	8.140	10.464	6.904	90.0	85.0	90.0	586
Monoclinic	11.446	8.103	6.077	90.0	86.7	90.0	563
Monoclinic	8.835	10.456	6.537	90.0	84.6	90.0	601
Monoclinic	6.781	11.198	9.219	90.0	116.8	90.0	625
Monoclinic	10.847	11.090	7.973	90.0	103.1	90.0	583
Monoclinic	8.152	11.015	7.330	90.0	95.5	90.0	655

**Table 3.2:** Possible lattice parameters of phase III generated according to the experimental XRD pattern at 11.44 GPa using DICVOL.

System	$a$ (Å)	$b$ (Å)	$c$ (Å)	$\alpha$ (°)	$\beta$ (°)	$\gamma$ (°)	$V$ (Å <sup>3</sup> )
Monoclinic	6.926	12.475	5.762	90.0	121.0	90.0	428
Monoclinic	7.597	7.952	8.241	90.0	104.6	90.0	482
Monoclinic	8.251	11.303	5.374	90.0	98.8	90.0	495
Monoclinic	7.253	9.879	7.089	90.0	118.0	90.0	447
Monoclinic	3.857	10.661	7.151	90.0	128.3	90.0	460
Monoclinic	8.139	10.597	5.827	90.0	88.2	90.0	502
Monoclinic	8.755	6.314	10.413	90.0	124.8	90.0	473
Monoclinic	11.041	3.859	10.686	90.0	86.4	90.0	454
Monoclinic	10.334	7.721	5.354	90.0	85.4	90.0	426
Monoclinic	9.625	4.369	10.831	90.0	108.2	90.0	433
Monoclinic	7.239	10.687	5.561	90.0	87.6	90.0	430
Monoclinic	7.737	8.176	6.873	90.0	85.4	90.0	433
Orthorhombic	11.785	5.400	7.832	90.0	90.0	90.0	498
Orthorhombic	12.358	3.803	10.171	90.0	90.0	90.0	475
Orthorhombic	11.704	10.562	4.074	90.0	90.0	90.0	504
Orthorhombic	3.812	11.609	10.880	90.0	90.0	90.0	482
Orthorhombic	6.176	5.538	14.178	90.0	90.0	90.0	485

### 3.2 Generation of candidate structures using USPEX

To generate initial atomic positions of possible candidate structures for crystal structure search simulations, we used the experimental values of bond lengths and angles of the EDAB molecule [109] at ambient pressure. We also used lattice parameters obtained from the DICVOL indexing software in order to narrow down the list. The USPEX package generated 825 candidate structures with 33 top-ranked structures for the two phases. The simulations show that there are 7 crystal



structures with relatively low enthalpies among all the candidates. They belong to 5 different space groups:  $C2/c$ ,  $Cc$ ,  $P2_1/c$ ,  $P2_1$  and  $P2_12_12_1$ . For the candidates with the same space group  $P2_1/c$  and  $P2_12_12_1$ , they are distinguished by labels A and B. The ambient-pressure crystal structures of these 7 candidates are shown in Figure 3.1. The cell parameters and Wyckoff positions for the primitive unit cells of the seven short-listed structures are listed in the Appendix.

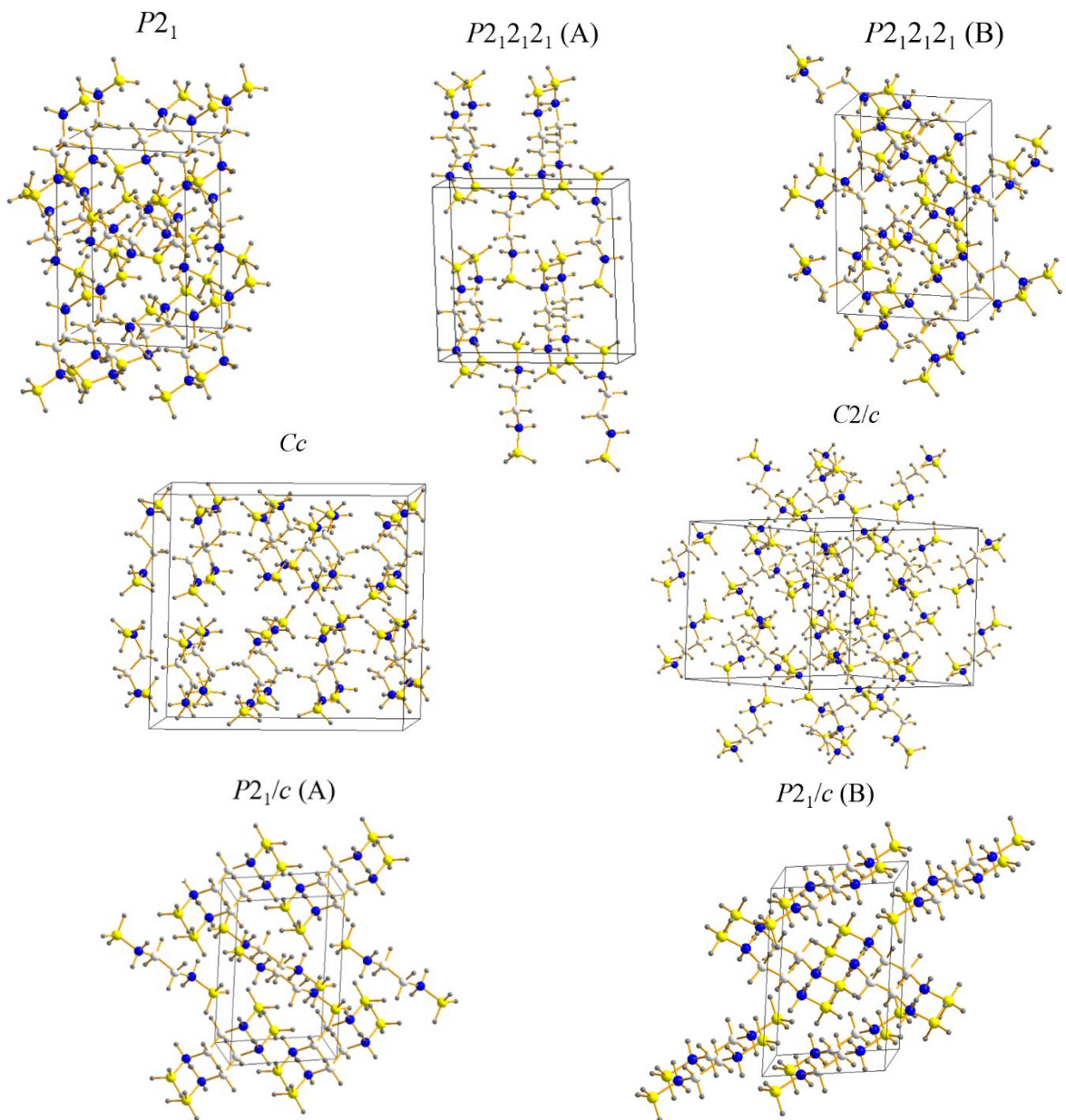


**Figure 3.1:** Crystal structures of the seven top-ranked candidates at ambient pressure.

# 4 Identification of the new high-pressure phases of EDAB

In order to determine the structures of the two high-pressure phases of EDAB, we calculated the pressure-enthalpy curves of the 7 top-ranked candidates and compared the simulated XRD patterns against the experimental XRD patterns at target pressures. The two new phases were thus found to have the same  $P2_1/c$  symmetry.

## 4.1 Pressure-enthalpy curves of EDAB candidates using the vdW-DF and PBE functionals

We used the vdW-DF and the PBE functional to calculate the pressure-enthalpy curves of seven top-ranked candidates. Figure 4.1 shows how the computed vdW-DF enthalpies of these structures vary with pressure. At ambient pressure, the experimental structure (space group:  $Pbca$ ) is the most stable one. It is about 0.012 eV/molecule lower by enthalpy than the  $P2_1/c$  (A) structure. All other structures are at least 0.22 eV/molecule higher than the experimental structure. Under compression to 0.20 GPa, the  $P2_1/c$  (A) structure becomes more stable than the experimental structure, indicating that the first phase transition may occur at this pressure. The  $P2_1/c$  (A) structure remains the most stable until about 8.50 GPa when the  $P2_1/c$  (B) structure overtakes the lead, indicating a second phase transition. The enthalpies of the  $P2_1/c$  (A) and  $P2_1/c$  (B) structures are very close at pressures higher than 8.0 GPa, the largest difference of enthalpies being 0.035 eV/molecule at 15.0 GPa. Moreover, these two structures share the same space group and differ only by cell dimensions. This suggests that these two  $P2_1/c$  structures may coexist during the second phase transition. The relative enthalpies of the candidates are listed in Table 4.1.

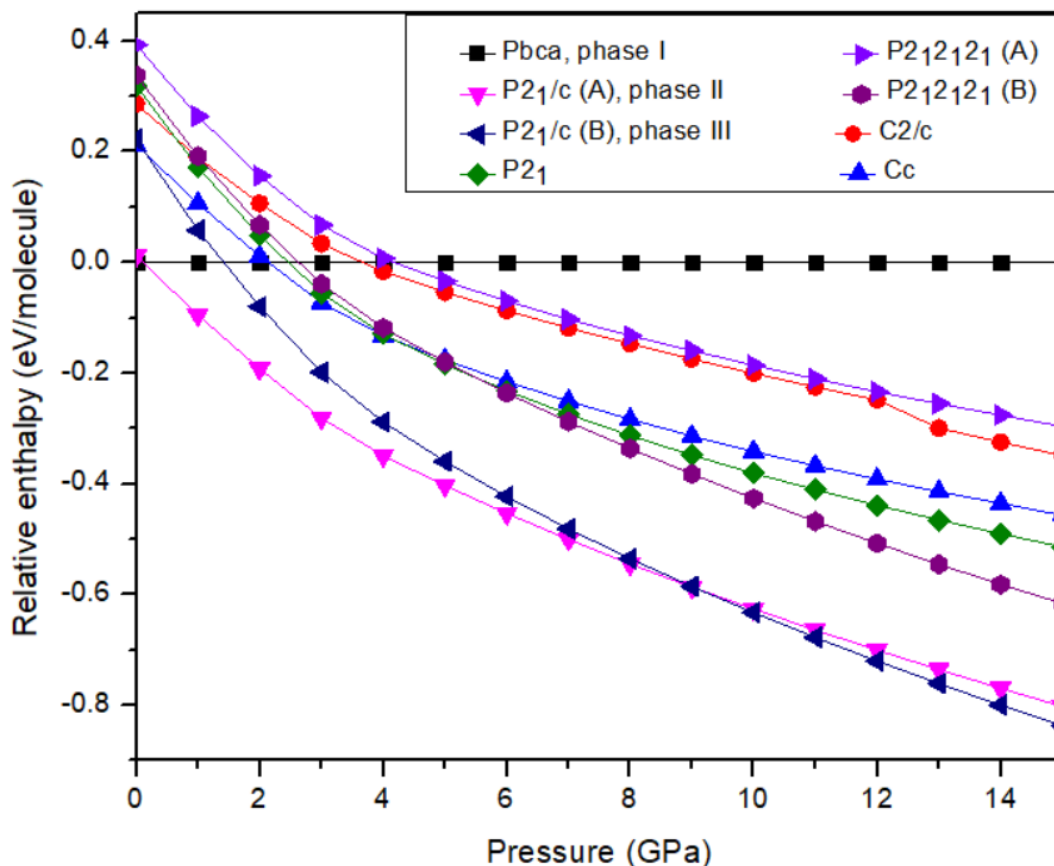


**Figure 4.1:** Calculated vdW-DF enthalpies of the seven candidate structures as functions of pressure, relative to the enthalpies of the reference EDAB structure.

It is instructive to compare the vdW-DF results with predictions of the simpler PBE functional. The pressure-enthalpy curves for the same seven candidate structures calculated using the PBE functional are shown in Figure 4.2 and Table 4.2. In terms of enthalpy, the PBE method also predicts that the  $P2_1/c$  (A) structure is the second most stable except for the experimental  $Pbca$  structure at ambient pressure. It is about 0.133 eV/molecule higher in enthalpy than the  $Pbca$  structure. At about 1.4 GPa, the  $P2_1/c$  (A) structure becomes more stable than the experimental structure, indicating the first phase transition. This  $P2_1/c$  (A) structure remains the most stable one until about 5.0 GPa, when the  $P2_1/c$  (B) structure surpasses it in stability, indicating the second phase transition. The experiments suggest that the first phase transition occurs at around 1.0 GPa and the second phase transition pressure near 8.0 GPa. Thus, the vdW-DF functional predicts phase transition pressures more accurately than the PBE functional.

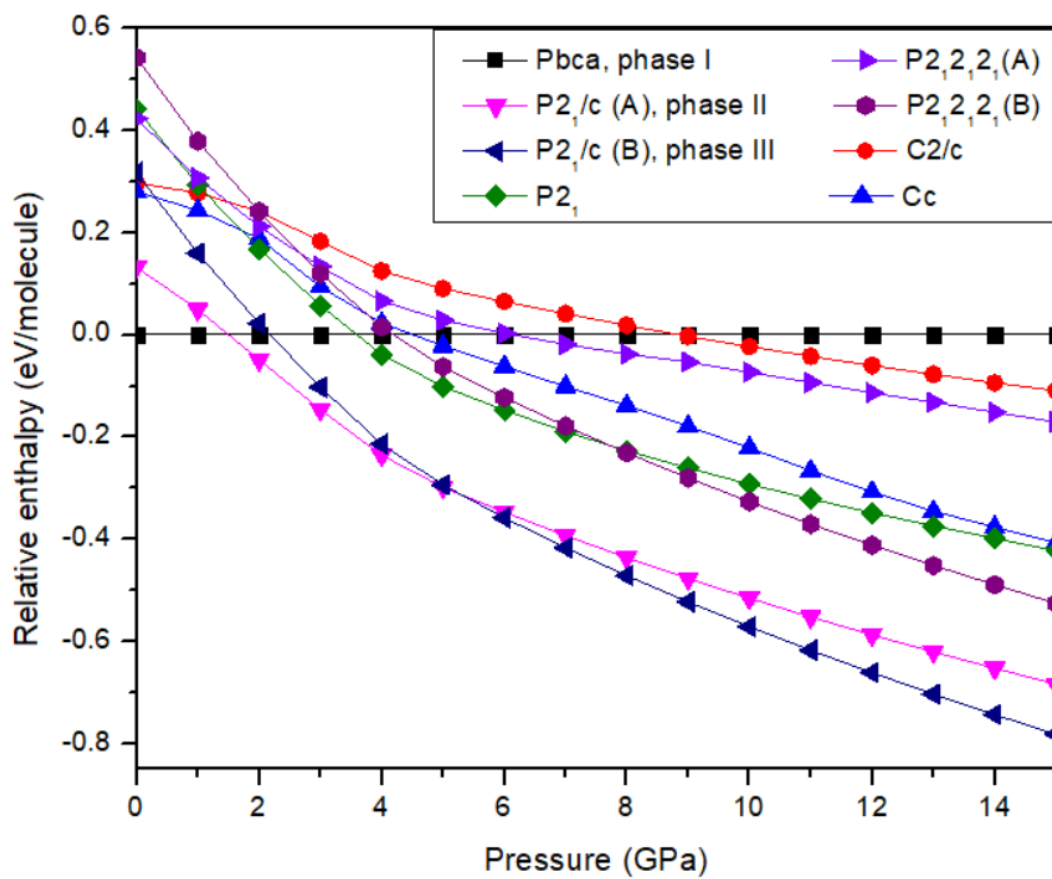


**Figure 4.2:** Calculated PBE enthalpies of the seven candidate structures as functions of pressure, relative to the enthalpies of the reference EDAB structure.

**Table 4.1:** Relative enthalpies (eV/molecule) as a function of pressure for seven candidate structures calculated using the vdW-DF functional.

$P$ (GPa)	Candidate structures						
	$C2/c$	$Cc$	$P2_1/c$ (A)	$P2_1$	$P2_1/c$ (B)	$P2_12_12_1$ (A)	$P2_12_12_1$ (B)
0	0.287	0.212	0.012	0.319	0.223	0.393	0.338
1	0.190	0.107	-0.095	0.172	0.058	0.264	0.192
2	0.107	0.012	-0.192	0.048	-0.080	0.156	0.068
3	0.034	-0.072	-0.281	-0.055	-0.198	0.068	-0.039
4	-0.016	-0.132	-0.349	-0.129	-0.288	0.007	-0.118
5	-0.053	-0.176	-0.403	-0.184	-0.359	-0.034	-0.180
6	-0.087	-0.215	-0.453	-0.232	-0.423	-0.070	-0.236
7	-0.118	-0.251	-0.500	-0.274	-0.481	-0.103	-0.288
8	-0.147	-0.283	-0.544	-0.312	-0.535	-0.132	-0.336
9	-0.174	-0.313	-0.586	-0.348	-0.585	-0.159	-0.382
10	-0.200	-0.341	-0.626	-0.381	-0.633	-0.186	-0.426
11	-0.225	-0.367	-0.664	-0.411	-0.677	-0.210	-0.468
12	-0.248	-0.391	-0.700	-0.438	-0.720	-0.233	-0.507
13	-0.299	-0.414	-0.735	-0.465	-0.761	-0.255	-0.545
14	-0.325	-0.435	-0.769	-0.490	-0.800	-0.276	-0.581
15	-0.349	-0.457	-0.802	-0.514	-0.837	-0.296	-0.616

**Table 4.2:** Relative enthalpies (eV/molecule) as a function of pressure for seven candidate structures calculated using the PBE functional.

$P$ (GPa)	Candidate structures						
	$C2/c$	$Cc$	$P2_1/c$ (A)	$P2_1$	$P2_1/c$ (B)	$P2_12_12_1$ (A)	$P2_12_12_1$ (B)
0	0.297	0.280	0.133	0.442	0.318	0.423	0.543
1	0.278	0.244	0.050	0.293	0.160	0.307	0.379
2	0.242	0.188	-0.048	0.168	0.022	0.212	0.242
3	0.183	0.094	-0.146	0.057	-0.102	0.133	0.120
4	0.125	0.023	-0.235	-0.038	-0.213	0.066	0.015
5	0.091	-0.022	-0.298	-0.101	-0.294	0.028	-0.062
6	0.065	-0.062	-0.346	-0.147	-0.358	0.003	-0.122
7	0.041	-0.101	-0.393	-0.189	-0.417	-0.019	-0.179
8	0.019	-0.138	-0.436	-0.226	-0.471	-0.037	-0.231
9	-0.003	-0.179	-0.476	-0.261	-0.522	-0.053	-0.280
10	-0.023	-0.221	-0.515	-0.292	-0.571	-0.073	-0.326
11	-0.042	-0.266	-0.552	-0.321	-0.617	-0.093	-0.370
12	-0.060	-0.307	-0.587	-0.348	-0.661	-0.113	-0.411
13	-0.077	-0.345	-0.620	-0.374	-0.703	-0.132	-0.451
14	-0.094	-0.376	-0.652	-0.398	-0.743	-0.151	-0.489
15	-0.109	-0.407	-0.683	-0.422	-0.781	-0.170	-0.525

In summary, our DFT calculations showed that EDAB undergoes a structural transformation from  $Pbca$  symmetry to  $P2_1/c$  symmetry near 1.0 GPa. A second phase transition of EDAB takes place at around 8.0 GPa within  $P2_1/c$ , and it remains the most stable structure until at least to 15.0 GPa.

## 4.2 Comparison between experimental and simulated XRD patterns

The simulated and experimental XRD patterns of the  $P2_1/c$  (A) and the  $P2_1/c$  (B) structures are shown in Figure 4.3 and Figure 4.4, respectively. The two pressures for comparisons are 1.72 and 11.44 GPa, at which the experimental patterns were the clearest. For the  $P2_1/c$  (A) phase at 1.72 GPa, the simulated and experimental XRD patterns match very well, indicating the  $P2_1/c$  (A) structure is the second phase of EDAB upon compression.

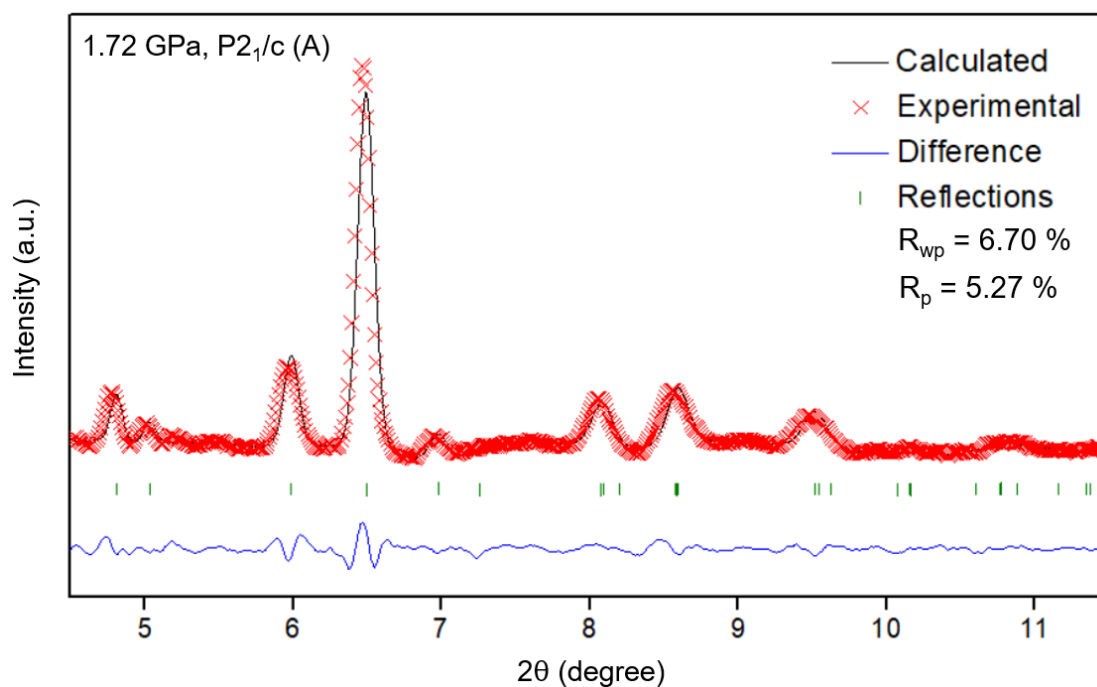


**Figure 4.3:** The simulated and experimental XRD spectra of the  $P2_1/c$  (A) structure at 1.72 GPa.

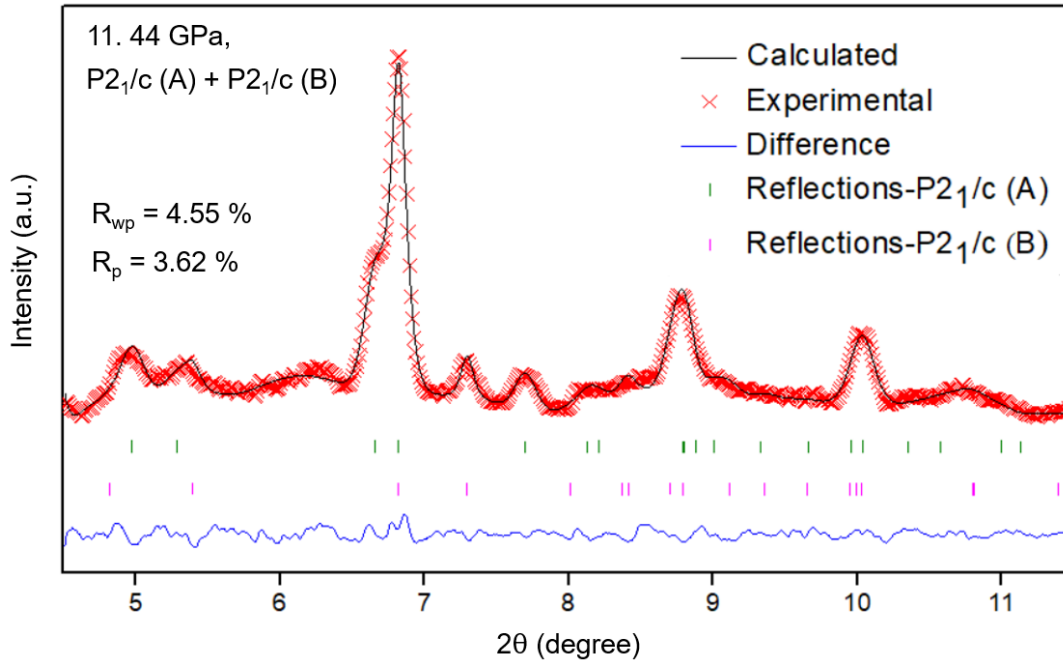


**Figure 4.4:** The simulated and experimental XRD spectra of the  $P2_1/c$  (A) and the  $P2_1/c$  (B) structures at 11.44 GPa.

Figure 4.4 suggests that the  $P2_1/c$  (A) and the  $P2_1/c$  (B) structures coexist at 11.44 GPa because the simulated and the experimental XRD patterns at this pressure are similar. This result is consistent with our DFT calculations. Thus, we conclude that EDAB exists as  $Pbca$  until around 1 GPa when it transforms into  $P2_1/c$  (A) structure. The second phase transition starts taking place at pressures higher than 8 GPa, and the  $P2_1/c$  (A) structure coexists with the  $P2_1/c$  (B) structure at least to 15 GPa. The experimental and theoretical lattice parameters for the three EDAB phases under high pressures are listed in Table 4.3 and Table 4.4, respectively.



**Table 4.3:** Experimental unit cell parameters of EDAB as a function of pressure.

$P$ (GPa)	Phase	$a$ (Å)	$b$ (Å)	$c$ (Å)	$\beta$ (°)	$V$ (Å <sup>3</sup> )
0.72	I	10.893	8.178	8.121	90.0	723.4
1.07	I	10.631	8.114	8.154	90.0	703.4
1.72	II	4.494	6.424	10.687	102.0	301.8
2.41	II	4.454	6.382	10.632	101.8	295.8
3.70	II	4.284	6.211	10.497	100.7	274.4
4.77	II	4.274	6.168	10.529	100.8	272.6
5.21	II	4.233	6.098	10.546	100.3	267.8
6.91	II	4.198	6.073	10.511	100.1	263.8
7.88	II	4.112	5.855	10.659	98.6	253.7
9.42	III	3.890	10.907	7.123	128.5	236.5
11.44	III	3.841	10.911	6.998	128.8	228.6
14.72	III	3.817	10.814	6.806	126.8	224.9

**Table 4.4:** Computational unit cell parameters of EDAB as a function of pressure.

$P$ (GPa)	Phase	$a$ (Å)	$b$ (Å)	$c$ (Å)	$\beta$ (°)	$V$ (Å <sup>3</sup> )
0	I	10.669	8.345	8.236	90.0	733.2
1	I	10.334	8.155	8.105	90.0	683.0
2	II	4.406	6.280	10.761	101.3	292.0
3	II	4.299	6.118	10.800	100.6	279.2
4	II	4.218	5.945	10.875	99.9	268.6
5	II	4.150	5.811	10.929	99.5	259.9
6	II	4.092	5.716	10.950	99.2	252.8
7	II	4.042	5.631	10.973	99.1	246.6
8	II	3.997	5.556	10.994	99.0	241.1
9	III	3.941	10.149	7.494	128.8	233.6
10	III	3.909	10.097	7.448	128.7	229.4
11	III	3.879	10.050	7.405	128.6	225.6
12	III	3.852	10.005	7.365	128.5	222.1
13	III	3.826	9.961	7.327	128.4	218.8
14	III	3.802	9.919	7.292	128.3	215.8
15	III	3.780	9.879	7.259	128.2	213.0

### 4.3 Equation of state for EDAB

In order to investigate mechanical properties of EDAB under high pressure in use of hydrogen storage materials, we applied equation of state for the compressibility. We used the third-order Birch–Murnaghan [136] isothermal equation of state for our three phases simulated by DFT calculations in a pressure range of 0–15 GPa. This equation of state is:

$$P(V) = \frac{3B_0}{2} \left[ \left( \frac{V_0}{V} \right)^{\frac{7}{3}} - \left( \frac{V_0}{V} \right)^{\frac{5}{3}} \right] \left\{ 1 + \frac{3}{4} (B_0' - 4) \left[ \left( \frac{V_0}{V} \right)^{\frac{2}{3}} - 1 \right] \right\}, \quad (4.1)$$

where  $P$  is the pressure,  $V_0$  is the reference volume,  $V$  is the deformed volume,  $B_0$  is the bulk modulus, and  $B_0'$  is the derivative of the bulk modulus with respect to pressure. Figure 4.5 shows the fitting curves of volume versus pressure, together with the corresponding experimental data of these three phases under high pressure. The results of the fit are summarized in Table 4.5. For phase I, the comparison of  $B_0$  and  $V_0$  values between calculations and experiments is not available because there are no experimental data. For phase II, the fitted  $B_0$  is 12.13 GPa, which is only 46% of the experimental value. This difference is mainly from the  $V_0$  values, which are  $156.82 \text{ \AA}^3$  for experiments and  $170.69 \text{ \AA}^3$  for calculations, respectively. For phase III, the calculated bulk modulus  $B_0$  is also smaller than the experimental  $B_0$ , although here the theoretical and experimental  $V_0$  values are relatively close. The difference is about 8.16 GPa. This error source is mainly from the pressure-volume curves in which all calculated volumes from 8 to 15 GPa are below the experimental ones. It indicates that theoretical phases are more compressible than the real ones. In addition, the discrepancy between calculations and experiments may be due to the coexistence of the  $P2_{1/c}$  (A) and  $P2_{1/c}$  (B) phases at pressures higher than 8 GPa. The equation of state clearly shows the phase transformations taking place in the EDAB upon compression.

**Table 4.5:** Comparison of experimental and computational data of equation of state in EDAB.

EDAB Phase	Experiment		Theory	
	$V_0$ ( $\text{\AA}^3$ )	$B_0$ (GPa)	$V_0$ ( $\text{\AA}^3$ )	$B_0$ (GPa)
Phase I ( $Pbca$ )	178.86	—	189.40	7.15
Phase II ( $P2_1/c$ (A))	156.82	26.58	170.69	12.13
Phase III ( $P2_1/c$ (B))	151.08	24.50	154.94	16.31

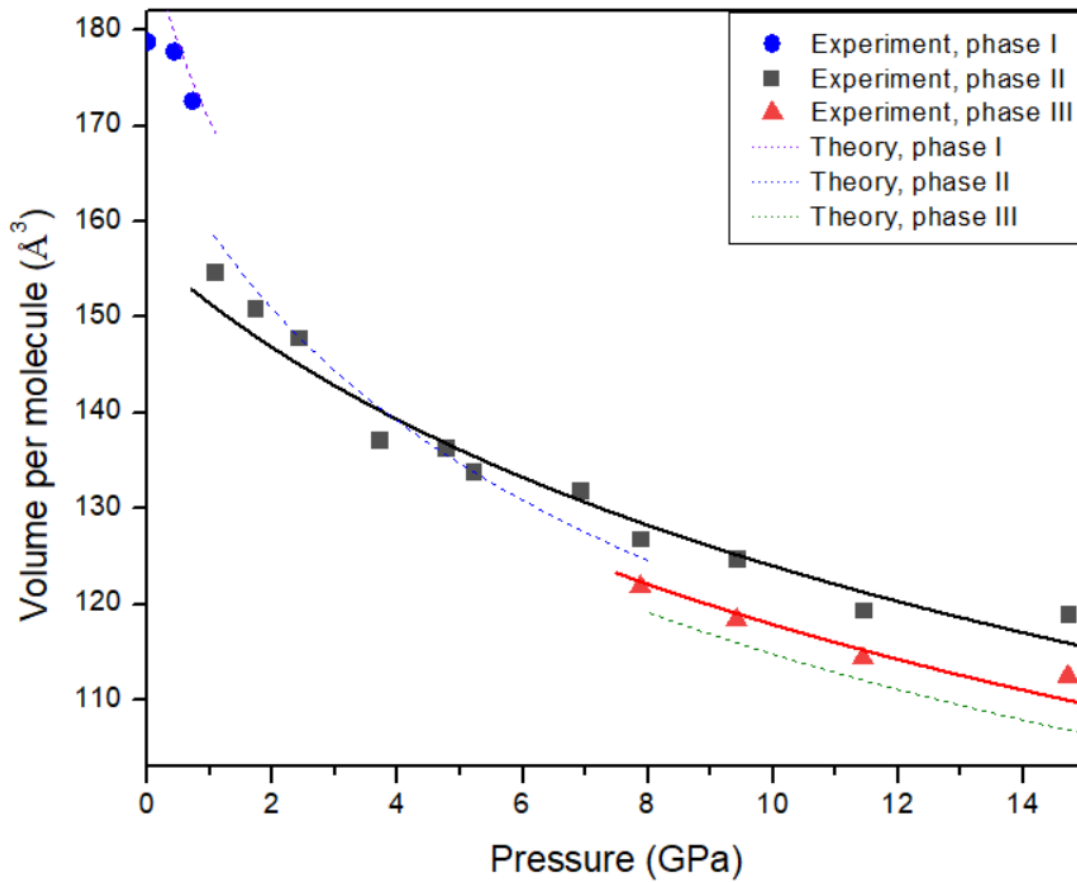


**Figure 4.5:** Experimental and theoretical equations of state for the EDAB phases obtained by fitting third-order Birch–Murnaghan equation of state.

# 5 Evolution of dihydrogen bonding frameworks in EDAB

Phase transitions of molecular crystals under compression are complicated chemical processes in which both inter- and intra-molecular interactions play a role. One particular type of intermolecular interaction possible between EDAB molecules involves weak N-H...H-B dihydrogen bonds. Chemically, the NH group is a protic acid, resulting in the hydrogen atom with a positive charge. In contrast, the borane end of BH is hydridic, leading to the hydrogen atom with a negative charge. The attraction interactions between two hydrogens of NH and BH groups from different EDAB molecules can be enhanced by high pressure, forming dihydrogen bonds. In addition, note that the electronegativity of nitrogen is relatively larger than that of boron. Thus, the evolution of dihydrogen bond angles under high pressure can be related to the electronegativity for phase transitions. Because dihydrogen bonds are involved in phase transformations, we decided to investigate how they evolve with increasing pressure.

## 5.1 The dihydrogen bonding frameworks of phase II

The criterion of dihydrogen bonding is based on the Cambridge structural database [75] that established an empirical rule: a hydrogen bond is said to exist when the H...H distance between two molecules falls in the range from 1.7 to 2.2 Å. In this study, we adopted the maximum distance of 2.2 Å in order to investigate the evolution of the dihydrogen bonding formation process induced by high pressure.

At ambient pressure, all of the N-H...H-B distances in the *Pbca* (ambient-pressure) structure of EDAB are greater than 2.2 Å, indicating that there are no dihydrogen bonds. At the pressure of about 2 GPa, we found eight dihydrogen bonds per molecule, as shown in Figure 5.1 (a). These eight bonds are equally divided into two types with different bond lengths and angles. We used the dashed lines of different colors to indicate the two types of dihydrogen bonds. At around 8 GPa, two more dihydrogen bonds are found (Figure 5.1 (b)). In fact, these two new bonds start to form at about 4 GPa, as shown in Figure 5.2 (a). Naturally, hydrogen bond lengths decrease upon compression. In Figure 5.2 (b), the N-H...H angle is relatively more linear (closer to 180°) while the B-H...H is more bent with a pressure increase due to the chemical properties of functional group NH and BH on the charge transfer capability. This will be discussed in detail in

Section 5.3. Thus, the formation of dihydrogen bonds under high pressure is also relevant to the types of functional groups.

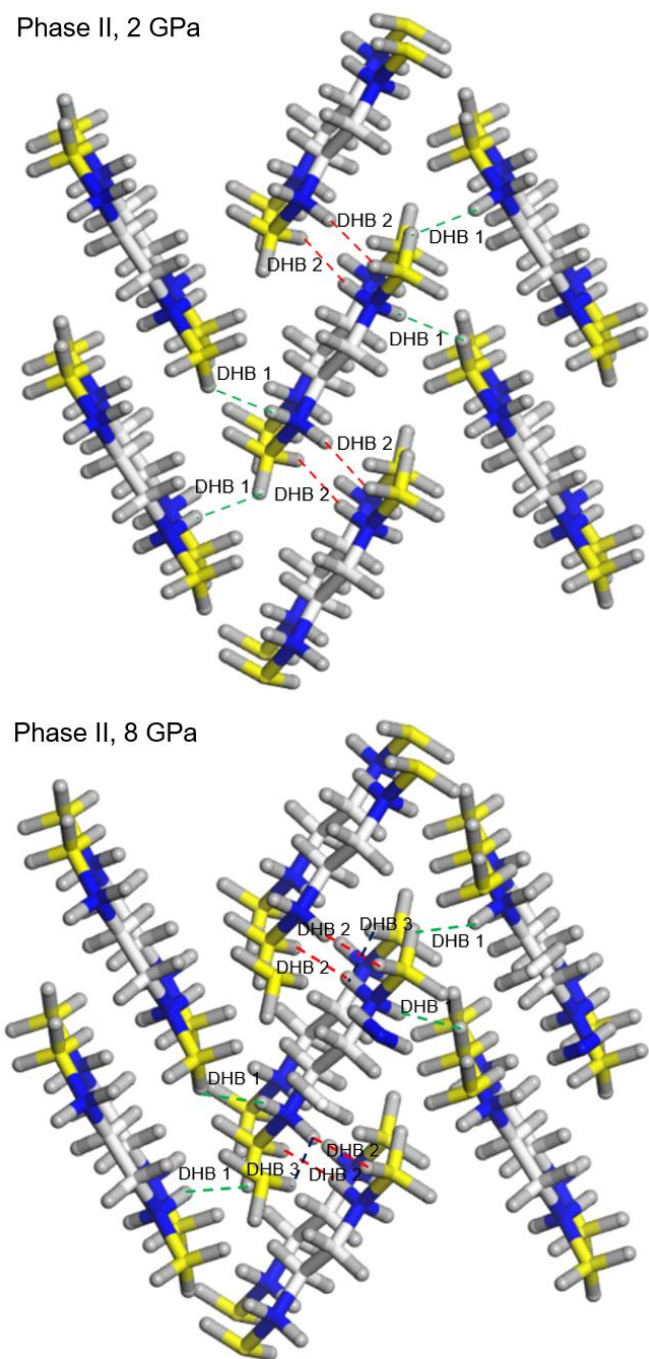


**Figure 5.1:** The dihydrogen bonding (N-H...H-B) frameworks (represented by dashed lines, and the color correspond to the type of bonds) between EDAB ( $B_2N_2C_2H_{14}$ ) molecules at 2 GPa (a) and 8 GPa (b).

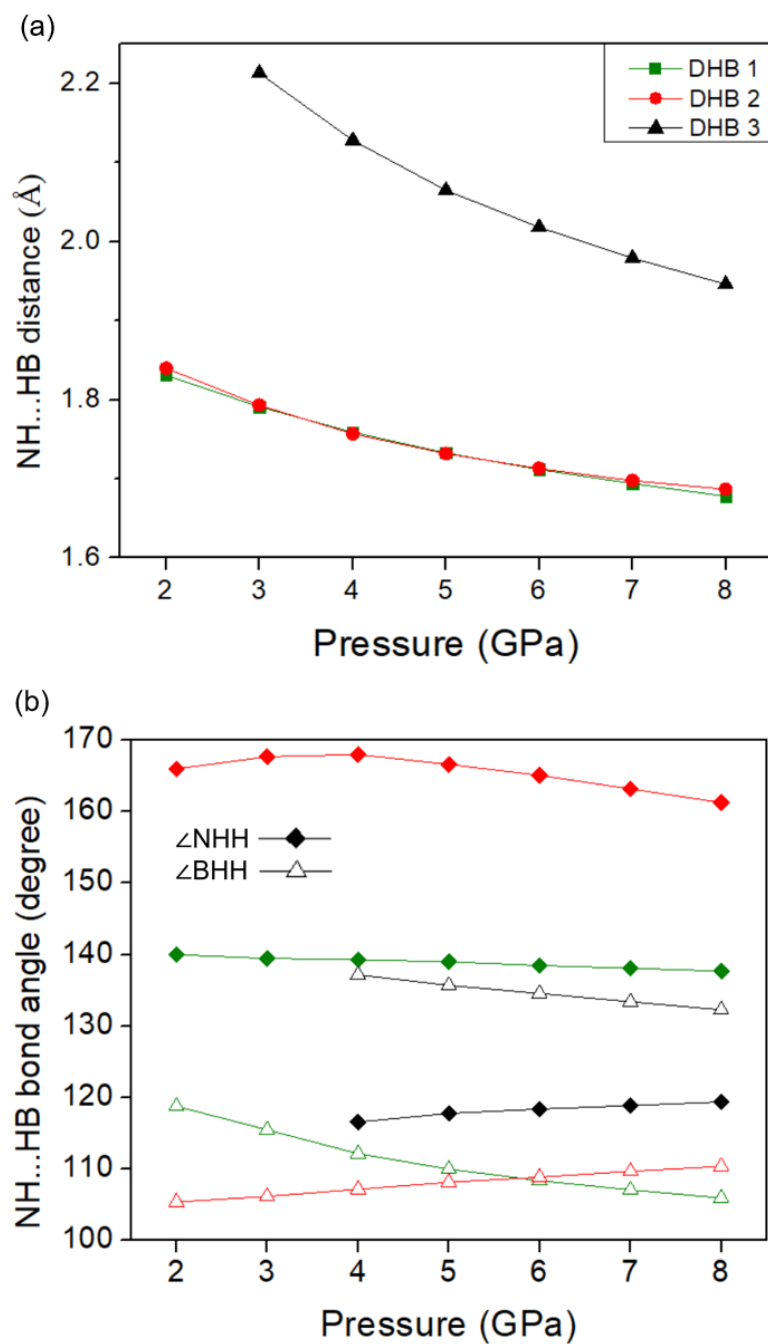


**Figure 5.2:** (a) The N-H...H-B distance versus pressure in phase II. The black dashed line represents the dihydrogen bonds length criterion. (b) The N-H...H and B-H...H angles versus pressure in phase II.

## 5.2 The dihydrogen bonding frameworks of phase III

The evolution of dihydrogen bonds in the  $P2_1/c$  (B) phase is shown in the Figure 5.3. Between 8 and 12 GPa, there are sixteen dihydrogen bonds naturally falling into four groups. At 12 GPa, a fifth group appears and the total number of dihydrogen bonds increases to twenty. Then the total number of dihydrogen bonds remained twenty up to 14 GPa.

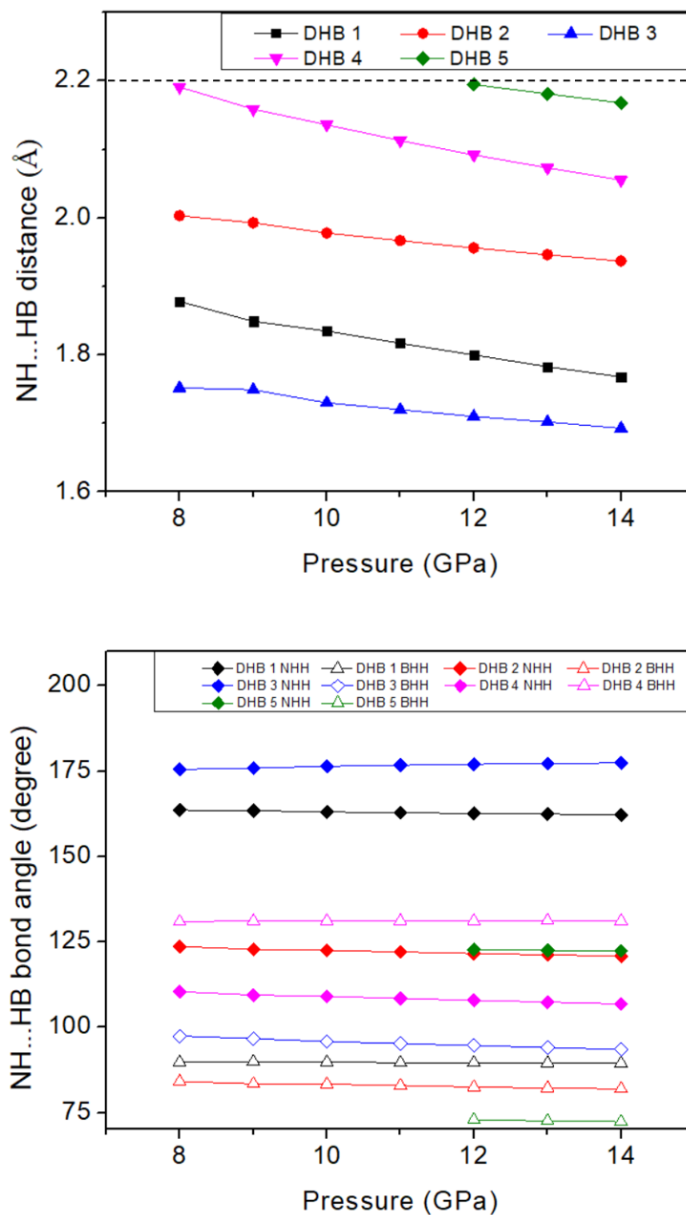


**Figure 5.3:** (a) The N-H...H-B distance versus pressure in phase III. (b) The N-H...H and B-H...H angles versus pressure in phase III.



### 5.3 The origin of the phase transformations in EDAB at high pressure

Chemically, dihydrogen bond is an interaction two hydrogen atoms, one of which belongs to a hydride group (such as BH) and the other to a proton-donor group (such as OH and NH). The interaction arises because hydride H atoms and H atoms of proton-donor groups carry opposite partial charges [137]. In the high-pressure phases of EDAB, dihydrogen bonds involve the NH and BH groups from different EDAB molecules. Thus, dihydrogen bonds are related to inter-molecular interactions. Their bond length changes for the formation process under high pressure are generally within about 0.4 Å. In comparison with intra-molecular bond lengths of N-H, B-H, and C-H, these covalent bond lengths remain almost unchanged under compression, as seen in Table 5.1. In addition, the Pauling electronegativity of boron is about 2.04, while for nitrogen it is 3.04. Consequently, the dihydrogen bond angles associated with B-H groups may be changed relatively significant than the ones associated with N-H groups due to pressure-induced charge transfer effects observed in large organic molecules [138]. The B-H groups can be active sites for phase transitions involving the formation of dihydrogen bonds under high pressure. In our DFT calculations, this is seen in the evolution of dihydrogen bond angles B-H...H in Figure 5.2 (b).

**Table 5.1:** Bond lengths of covalent N-H, B-H and C-H in EDAB molecules under high pressure

	Phase I		Phase II		Phase III	
	0 GPa	2 GPa	2 GPa	8 GPa	8 GPa	14 GPa
$R(\text{N-H})$ (Å)	1.029	1.027	1.028	1.027	1.027	1.026
$R(\text{B-H})$ (Å)	1.217	1.215	1.211	1.201	1.200	1.192
$R(\text{C-H})$ (Å)	1.095	1.093	1.094	1.090	1.090	1.087

The evolution of dihydrogen bonds in EDAB under pressure shows that the number of dihydrogen bonds increased from zero in the orthorhombic  $Pbca$  phase to eight in the monoclinic  $P2_1/c$  (A) phase at 2 GPa. As the pressure is raised to 8 GPa, the number of dihydrogen bonds increases from eight in the monoclinic  $P2_1/c$  (A) phase to sixteen in the monoclinic  $P2_1/c$  (B) phase. These results indicate that the phase transitions in EDAB under high pressures are accompanied by the formation of dihydrogen bond frameworks.

## 6 Summary and outlook

The experimental results from the Song group [114] suggested two phase transitions of EDAB occurring at 1 and 8 GPa. In order to determine the crystal structures of the new phases, we employed DFT calculations. Our results show that EDAB undergoes a phase transition from orthorhombic  $Pbca$  to monoclinic  $P2_1/c$  at around 1 GPa. A second phase transformation takes place at around 8 GPa within  $P2_1/c$ , and the two phases coexist up to at least 15 GPa. We also investigated the N-H...H-B dihydrogen bonding network evolution of EDAB upon compression. In the  $P2_1/c$  (A) phase, the number of dihydrogen bonds increases from 8 to 10 in the pressure range from 2 to 8 GPa. In the  $P2_1/c$  (B) phase, the number of dihydrogen bonds increases from 16 to 20 at 12 GPa and remains the same amount up to 14 GPa. The origin of the phase transitions is attributed to the formation of dihydrogen bond frameworks.

Our calculations show that the formation of dihydrogen bonds at high pressure is closely linked to the chemical properties of the NH and BH functional groups and involves charge transfer. The N-H...H dihydrogen bonds are almost linear, remaining almost unchanged under high pressure in comparison of the B-H...H dihydrogen bonds, which are bent. This indicates that BH groups in molecular EDAB crystals become active under high pressure. Consequently, the origin of high-pressure induced phase transitions can also be attributed to evolutionary changes associated with dihydrogen bond angles of the B-H...H.

In future work, we will perform DFT calculations to investigate the dynamic evolution of the dihydrogen bond formation and dihydrogen bond angle changes under high pressure for phase transitions.

# Bibliography

- [1] J. V. Badding. High-pressure synthesis, characterization, and tuning of solid state materials. *Annu. Rev. Mater. Sci.* **28**, 631 (1998).
- [2] R. J. Hemley. Effects of high pressure on molecules. *Annu. Rev. Phys. Chem.* **51**, 763 (2000).
- [3] P. F. McMillan. New materials from high-pressure experiments. *Nat. Mater.* **1**, 19 (2002).
- [4] P. F. McMillan. New materials from high-pressure experiments: Challenges and opportunities. *High Press. Res.* **23**, 7 (2003).
- [5] P. F. McMillan. Condensed matter chemistry under extreme high pressure high temperature conditions. *High Press. Res.* **24**, 67 (2004).
- [6] P. F. McMillan. Pressing on: The legacy of Percy W. Bridgman. *Nat. Mater.* **4**, 715 (2005).
- [7] P. F. McMillan. Chemistry at high pressure. *Chem. Soc. Rev.* **35**, 855 (2006).
- [8] P. F. McMillan, M Wilson, D. Daisenberger and D. Machon. A density-driven phase transition between semiconducting and metallic polyamorphs of silicon. *Nat. Mater.* **4**, 680 (2015).
- [9] P. Wang, J. Guan, D. T. K Galeschuk, Y. Yao, C. F. He, S. Jiang, S. Zhang, Y. Liu, M. Jin, C. Jin and Y. Song. Pressure-induced polymorphic, optical, and electronic transitions of formamidinium lead iodide perovskite. *J. Phys. Chem. Lett.* **8**, 2119 (2017).
- [10] X. Cheng, D. Guo, Shi. Feng, K. Yang, Y. Wang, Y. Ren and Y. Song. Structure and stability of monazite-and zircon-type  $\text{LaVO}_4$  under hydrostatic pressure. *Opt. Mater.* **49**, 32 (2015).
- [11] F. Xiao, Z. Dong, H. Mao, J. Liu, X. Sun and Y. Song. Morphology and lattice stability-dependent performance of nanostructured  $\text{Li}_4\text{Ti}_5\text{O}_{12}$  probed by *in situ* high-pressure Raman spectroscopy and synchrotron X-ray diffraction. *CrystEngComm.* **18**, 736 (2016).
- [12] L. Zhang, Y. Wang, J. Lv and Y. Ma. Materials discovery at high pressures. *Nat. Rev. Mater.* **2**, 1 (2017).

- [13] W. B. Holzapfel. Physics of solids under strong compression. *Rep. Prog. Phys.* **59**, 28 (1996).
- [14] A. Mujica, A. Rubio, A. Muz and R. J. Needs. High-pressure phases of group-IV, III–V, and II–VI compounds. *Rev. Mod. Phys.* **75**, 863 (2003).
- [15] H. K. Mao and R. J. Hemley. Ultrahigh-pressure transitions in solid hydrogen. *Rev. Mod. Phys.* **66**, 671 (1994).
- [16] C. Mailhot, L. H. Yang and A. K. McMahan. Polymeric nitrogen. *Phys. Rev. B* **46**, 14419 (1992).
- [17] M. I. Eremets, A. G. Gavriliuk, I. A. Trojan, D. A. Dzivenko and R. Boehler. Single-bonded cubic form of nitrogen. *Nat. Mater.* **3**, 558 (2004).
- [18] A. P. Drozdov, P. P. Kong, V. S. Minkov, S. P. Besedin, M. A. Kuzovnikov, S. Mozaffari, L. Balicas, F. F. Balakirev, D. E. Graf, V. B. Prakapenka, E. Greenberg, D. A. Knyazev, M. Tkacz and M. I. Eremets. Superconductivity at 250 K in lanthanum hydride under high pressures. *Nature* **569**, 528 (2019).
- [19] N. W. Ashcroft, in *Theory of dense hydrogen: proton pairing. From quantum mechanics to technology* (Springer, Berlin, 1996), pp. 1–22.
- [20] N. Dubrovinskaia and L. Dubrovinsky. Terapascal static pressure generation with ultrahigh yield strength nanodiamond. *Sci. Adv.* **2**, 1600341 (2016).
- [21] J. S. Tse. A chemical perspective on high pressure crystal structures and properties. *Natl. Sci. Rev.* **7**, 149 (2020).
- [22] A. Zeidler and W. A. Crichton. Materials under pressure. *MRS Bull.* **42**, 710 (2017).
- [23] E. Soignard and P. F. McMillan. An introduction to diamond anvil cells and loading techniques. *High-Pressure Crystallogr.* **81**, 100 (2004).
- [24] L. Dubrovinsky, N. Dubrovinskaia, V. B. Prakapenka and A. M. Abakumov. Implementation of micro-ball nanodiamond anvils for high-pressure studies above 6 Mbar. *Nat. Commun.* **3**, 1163 (2012).

- [25] L. Dubrovinsky, N. Dubrovinskaia, E. Bykova, M. Bykov, V. Prakapenka, C. Prescher, K. Glazyrin, H. P. Liermann, M. Hanfland, M. Ekholm, Q. Feng, L. V. Pourovskii, M. I. Katsnelson, J. M. Wills and I. A. Abrikosov. The most incompressible metal osmium at static pressures above 750 gigapascals. *Nature* **525**, 226 (2015).
- [26] Z. Dong. High-pressure study of molecular solids and 1D nanostructures by vibrational spectroscopy and synchrotron x-ray diffraction. *Electronic Thesis and Dissertation Repository*, Western University (2012).
- [27] Y. Lin, H. Ma, C. W. Matthews, B. Kolb, S. Sinogeikin, T. Thonhauser and W. L. Mao. Experimental and theoretical studies on a high pressure monoclinic phase of ammonia borane. *J. Phys. Chem. C* **116**, 2172 (2012).
- [28] S. Xie, Y. Song and Z. Liu. *In situ* high-pressure study of ammonia borane by Raman and IR spectroscopy. *Can. J. Chem.* **87**, 1235 (2009).
- [29] A. Torabi, C. Murli, Y. Song and V. N. Staroverov. Polymorphic transitions of diborane at sub-and near-megabar pressures. *Sci. Rep.* **5**, 13929 (2015).
- [30] S. Trudel and D. F. R. Gilson. High-pressure Raman spectroscopic study of the ammonia-borane complex. Evidence for the dihydrogen bond. *Inorg. Chem.* **42**, 2814 (2003).
- [31] G. Qi, K. Wang, K. Yang, and B. Zou. Pressure-induced phase transition of hydrogen storage material hydrazine bisborane: Evolution of dihydrogen bonds. *J. Phys. Chem. C* **120**, 21293 (2016).
- [32] M. Ramzan, T. Hussain and R. Ahuja, High pressure phase determination and electronic properties of lithiumamidoborane. *Appl. Phys. Lett.* **101**, 11902 (2012).
- [33] Q. Zhu, A. R. Oganov, M. A. Salvadó, P. Perterra and A. O. Lyakhov. Denser than diamond: *Ab initio* search for superdense carbon allotropes. *Phys. Rev. B* **83**, 193410 (2011).
- [34] M. Ramzan, F. Silvearv, A. Blomqvist, R. H. Scheicher, S. Lebègue and R. Ahuja. Structural and energetic analysis of the hydrogen storage materials  $\text{LiNH}_2\text{BH}_3$  and  $\text{NaNH}_2\text{BH}_3$  from *ab initio* calculations. *Phys. Rev. B* **79**, 132102 (2009).

- [35] S. M. Lee, X. D. Kang, P. Wang, H. M. Cheng and Y. H. Lee. A comparative study of the structural, electronic, and vibrational properties of  $\text{NH}_3\text{BH}_3$  and  $\text{LiNH}_2\text{BH}_3$ : Theory and experiment. *ChemPhysChem* **10**, 1825 (2009).
- [36] D. J. Wolstenholme, J. T. Titah, F. N. Che, K. T. Traboulosee, J. Flogeras, G. S. McGrady. Homopolar dihydrogen bonding in alkali-metal amidoboranes and its implications for hydrogen storage. *J. Am. Chem. Soc.* **133**, 16598 (2011).
- [37] W. Li, G. Wu, Y. Chua, Y. P. Feng and P. Chen. Role of  $\text{NH}_3$  in the dehydrogenation of calcium amidoborane ammoniate and magnesium amidoborane ammoniate: A first-principles study. *Inorg. Chem.* **51**, 76 (2012).
- [38] K. Wang, V. Arcisauskaite, J. S. Jiao, J. G. Zhang, T. L. Zhang and Z. N. Zhou. Structural prediction, analysis and decomposition mechanism of solid  $\text{M}(\text{NH}_2\text{BH}_3)_n$  ( $\text{M} = \text{Mg}, \text{Ca}$  and  $\text{Al}$ ). *RSC Adv.* **4**, 14624 (2014).
- [39] A. Torabi, Y. Song and V. N. Staroverov. Pressure-induced polymorphic transitions in crystalline diborane deduced by comparison of simulated and experimental vibrational spectra. *J. Phys. Chem. C* **117**, 2210 (2013).
- [40] A. M. Murcia Rios, D. N. Komsa and V. N. Staroverov. Effects of dispersion corrections and nonlocality on density functional predictions of pressure-induced polymorphic transitions of crystalline diborane. *J. Phys. Chem. C* **122**, 14781 (2018).
- [41] A. El Kharbachi, E. M. Dematteis, K. Shinzato, S. C. Stevenson, L. J. Bannenberg, M. Heere, C. Zlotea, P. A. Szilagy, J. P. Bonnet, W. Grochala, D. H. Gregory, T. Ichikawa, M. Baricco and B. C. Hauback. Metal hydrides and related materials. Energy carriers for novel hydrogen and electrochemical storage. *J. Phys. Chem. C* **124**, 7599 (2020).
- [42] F. Chang, H. Wu, R. Pluijm, J. Guo, P. Ngene and P. E. de Jongh. Effect of pore confinement of  $\text{NaNH}_2$  and  $\text{KNH}_2$  on hydrogen generation from ammonia. *J. Phys. Chem. C* **123**, 21487 (2016).

- [43] A. V. Ledovskikh and M. Wagemaker. Lattice-gas model for energy storage materials: Phase diagram and equilibrium potential as a function of nanoparticle size. *J. Phys. Chem. C* **120**, 11192 (2016).
- [44] M. Rueda, L. Sanz-Moral, J. J. Segovia and Á. Martín. Enhancement of hydrogen release kinetics from ethane 1,2 diamineborane (EDAB) by micronization using supercritical antisolvent (SAS) precipitation. *Chem. Eng. J.* **306**, 164 (2016).
- [45] S. Akbayrak and S. Özkar. Ammonia borane as hydrogen storage materials. *Int. J. Hydrog. Energy* **43**, 18592 (2018).
- [46] A. Staubitz, A. P. M. Robertson and I. Manners. Ammonia-borane and related compounds as dihydrogen sources. *Chem. Rev.* **110**, 4079 (2010).
- [47] W. T. Klooster, T. F. Koetzle, P. E. M. Siegbahn, T. B. Richardson and R. H. Crabtree. Study of the N-H...H-B dihydrogen bond including the crystal structure of  $\text{BH}_3\text{NH}_3$  by neutron diffraction. *J. Am. Chem. Soc.* **121**, 6337 (1999).
- [48] Y. J. Choi, E. Rönnebro, S. Rassat, A. Karkamkar, G. Maupin, J. Holladay, K. Simmons and K. Brooks. Kinetics study of solid ammonia borane hydrogen release-modeling and experimental validation for chemical hydrogen storage. *Phys. Chem. Chem. Phys.* **16**, 7959 (2014).
- [49] Song. Y. New perspectives on potential hydrogen storage materials using high pressure. *Phys. Chem. Chem. Phys.* **15**, 14524 (2013).
- [50] M. E. Bowden, G. J. Gainsford and W. T. Robinson. Room-temperature structure of ammonia borane. *Aust. J. Chem.* **60**, 149 (2007).
- [51] R. Custelcean and Z. A. Dreger. Dihydrogen bonding under high pressure: A Raman study of  $\text{BH}_3\text{NH}_3$  molecular crystal. *J. Phys. Chem. B* **107**, 9231 (2003).
- [52] S. Trudel and D. F. Gilson. High-pressure Raman spectroscopic study of the ammonia-borane complex. Evidence for the dihydrogen bond. *Inorg. Chem.* **42**, 2814 (2003).

- [53] Y. Lin, W. L. Mao, V. Drozd, J. Chen and L. L. Daemen. Raman spectroscopy study of ammonia borane at high pressure. *J. Chem. Phys.* **129**, 234509 (2008).
- [54] Y. Filinchuk, A. H. Nevidomskyy, D. Chernyshov and V. Dmitriev. High-pressure phase and transition phenomena in ammonia borane  $\text{NH}_3\text{BH}_3$  from X-ray diffraction, Landau theory, and *ab initio* calculations. *Phys. Rev. B* **79**, 214111 (2009).
- [55] J. Chen, H. Couvy, H. Liu, V. Drozd, L. L. Daemen, Y. Zhao, and C. C. Kao. *In situ* X-ray study of ammonia borane at high pressures. *Int. J. Hydrog. Energy* **35**, 11064 (2010).
- [56] R. S. Kumar, X. Ke, J. Zhang, Z. Lin, S. C. Vogel, M. Hartl, S. Sinogeikin, L. Daemen, A. L. Cornelius, C. Chen and Y. Zhao. Pressure induced structural changes in the potential hydrogen storage compound ammonia borane: A combined X-ray, neutron and theoretical investigation. *Chem. Phys. Lett.* **495**, 203 (2010).
- [57] A. Liu and Y. Song. *In situ* high-pressure and low-temperature study of ammonia borane by Raman spectroscopy. *J. Phys. Chem. C* **116**, 2123 (2012).
- [58] I. Kuppenko, L. Dubrovinsky, V. Dmitriev and N. Dubrovinskaia. *In situ* Raman spectroscopic study of the pressure induced structural changes in ammonia borane. *J. Chem. Phys.* **137**, 074506 (2012).
- [59] Y. Liang and J. S. Tse. First-principles study on the mechanisms for  $\text{H}_2$  formation in ammonia borane at ambient and high pressure. *J. Phys. Chem. C* **116**, 2146 (2012).
- [60] Y. Yao, X. Yong, J. S. Tse and M. J. Greschner. Dihydrogen bonding in compressed ammonia borane and its roles in structural stability. *J. Phys. Chem. C* **118**, 29591 (2014).
- [61] S. Aldridge, A. J. Downs, C. Y. Tang, S. Parsons, M. C. Clarke, R. D. L. Johnstone, H. E. Robertson, D. W. H. Rankin and D. A. Wann. Structures and aggregation of the methylamine-borane molecules,  $\text{Me}_n\text{H}_{3-n}\text{N}\cdot\text{BH}_3$  ( $n = 1-3$ ), studied by X-ray diffraction, gas-phase electron diffraction, and quantum chemical calculations. *J. Am. Chem. Soc.* **131**, 2231 (2009).
- [62] G. N. Patwari, T. Ebata and N. Mikami. Dehydrogenation reaction from a dihydrogen bonded precursor complex in the gas phase. *J. Phys. Chem. A* **105**, 10753 (2001).



- [63] M. E. Sloan, A. Staubitz, T. J. Clark, C. A. Russell, G. C. Lloyd-Jones and I. Manners. Homogeneous catalytic dehydrocoupling/dehydrogenation of amine-borane adducts by early transition metal, group 4 metallocene complexes. *J. Am. Chem. Soc.* **132**, 3831 (2010).
- [64] Z. T. Xiong, C. K. Yong, G. T. Wu, P. Chen, W. Shaw, A. Karkamkar, T. Autrey, M. O. Jones, S. R. Johnson, P. P. Edwards and W. I. F. David. High-capacity hydrogen storage in lithium and sodium amidoboranes. *Nat. Mater.* **7**, 138 (2008).
- [65] H. Wu, W. Zhou and T. Yildirim. Alkali and alkaline-earth metal amidoboranes: Structure, crystal chemistry, and hydrogen storage properties. *J. Am. Chem. Soc.* **130**, 14834 (2008).
- [66] T. E. Stennett and S. Harder. s-Block amidoboranes: syntheses, structures, reactivity and applications. *Chem. Soc. Rev.* **45**, 1112 (2016).
- [67] Y. S. Zhang and C. Wolverton. Crystal structures, phase stabilities, and hydrogen storage properties of metal amidoboranes. *J. Phys. Chem. C* **116**, 14224 (2012).
- [68] Z. T. Xiong, G. T. Wu, Y. S. Chua, J. J. Hu, T. He, W. L. Xu and P. Chen. Synthesis of sodium amidoborane ( $\text{NaNH}_2\text{BH}_3$ ) for hydrogen production. *Energy Environ. Sci.* **1**, 360 (2008).
- [69] K. J. Fijalkowski, R. V. Genova, Y. Filinchuk, A. Budzianowski, M. Derzsi, T. Jaron, P. J. Leszczynski and W. Grochala.  $\text{NaLi}(\text{NH}_2\text{BH}_3)_2$  — the first mixed-cation amidoborane with unusual crystal structure. *Dalton Trans.* **40**, 4407 (2011).
- [70] R. Owarzany, P. J. Leszczynski, K. T. Fijalkowski and W. Grochala. Mono- and bimetallic amidoboranes. *Crystals* **6**, 88 (2016).
- [71] Y. S. Chua, P. Chen, G. Wu, G and Z. Xiong. Development of amidoboranes for hydrogen storage. *ChemComm.* **47**, 5116 (2011).
- [72] H. Yamawaki, H. Fujihisa, Y. Gotoh, and S. Nakano. Structure of intermediate phase II of  $\text{LiNH}_2$  under high pressure. *J. Phys. Chem. B* **118**, 9991 (2014).

- [73] A. K. Mishra, T. Muramatsu, H. Liu, Z. M. Geballe, M. Somayazulu, M. Ahart, M. Baldini, Y. meng, E. Zurek and R. J. Hemley. New calcium hydrides with mixed atomic and molecular hydrogen. *J. Phys. Chem. C* **122**, 19370 (2018).
- [74] I. Errea, F. Belli, L. Monacelli, A. Sanna, T. Koretsune, T. Tadano, R. Bianco, M. Calandra, R. Arita, F. Mauri and J. A. flores-Lives. Quantum crystal structure in the 250-kelvin superconducting lanthanum hydride. *Nature* **578**, 66 (2020).
- [75] T. Richardson, S. de Gala, R. H. Crabtree and P. EM Siegbahn. Unconventional hydrogen bonds: Intermolecular BH. cntdot.. cntdot.. cntdot. HN interactions. *J. Am. Chem. Soc.* **51**, 12875 (1995).
- [76] D. J. Heldebrant, A. Karkamkar, N. J. Hess, M. Bowden, S. Rassat, F. Zheng, K. Rappe and T. Autrey. The effects of chemical additives on the induction phase in solid-state thermal decomposition of ammonia borane. *Chem. Mater.* **16**, 5332 (2008).
- [77] G. N. Patwari. Proton affinities of borane-amines: consequences on dihydrogen bonding. *J. Phys. Chem. A* **109**, 2035 (2005).
- [78] P. Giannozzi *et al.* QUANTUM ESPRESSO: A modular and open-source software project for quantum simulations of materials. *J. Phys. Condens. Matter.* **21**, 395502 (2009).
- [79] G. Kresse and J. Furthmüller. Efficient iterative schemes for *ab initio* total-energy calculations using a plane-wave basis set. *Phys. Rev. B* **54**, 11169 (1996).
- [80] S. J. Clark, M. D. Segall, C. J. Pickard, P. J. Hasnip, M. IJ Probert, K. Refson and M. C. Payne. First principles methods using CASTEP. *Z. Kristallogr. Cryst. Mater.* **220**, 567 (2005).
- [81] R. Car and M. Parrinello. Unified approach for molecular dynamics and density-functional theory. *Phys. Rev. Lett.* **55**, 2471 (1985).
- [82] R. Dovesi, R. Orlando, B. Civalleri, C. Roetti, V. R. Saunders and C. M. Zicovich–Wilson. CRYSTAL: A computational tool for the *ab initio* study of the electronic properties of crystals. *Z. Kristallogr. Cryst. Mater.* **220**, 571 (2005).

- [83] T. D. Kühne, M. Iannuzzi, M. Del Ben, V. V. Rybkin, P. Seewald, F. Stein, T. Laino, R. Z. Khaliullin, O. Schütt, F. Schiffmann, D. Golze, J. Wilhelm, S. Chulkov, M. H. B. Hashemian, V. weber, U. Borstnik, M. Taillefumier, A. S. Jakobovits, A. Lazzaro, H. Pabst, T. Müller, R. Schade, M. Guidon, S. Andermatt, N. Holmberg, G. K. schenter, A. Hehn, A. Bussy, F. Belleflamme, G. Tabacchi, A. Glob, M. Lass, I. Bethune, C. J. Mundy, C. Plessl, M. watkins, J. V. Vondele, M. Krack and J. Hutter. CP2K: An electronic structure and molecular dynamics software package-quickstep: Efficient and accurate electronic structure calculations. *J. Chem. Phys.* **152**, 194103 (2020).
- [84] J. M. Soler, E. Artacho, J. D. Gale, A. García, J. Junquera, P. Ordejón and D. Sánchez-Portal. The SIESTA method for *ab initio* order-N materials simulation. *J. Condens. Matter Phys.* **14**, 2745 (2002).
- [85] I. Errea, M. Calandra, C. J. Pickard, J. Nelson, R. J. Needs, Y. Li, H. Liu, Y. zhang, Y. Ma and F. Mauri. High-pressure hydrogen sulfide from first principles: A strongly anharmonic phonon-mediated superconductor. *Phys. Rev. Lett.* **114**, 157004 (2015).
- [86] H. Liu, I. I. Naumov, R. Hoffmann, N. W. Ashcroft and R. J. Hemley. Potential high- $T_c$  superconducting lanthanum and yttrium hydrides at high pressure. *Proc. Natl. Acad. Sci.* **114**, 6990 (2017).
- [87] X. Wen, R. Hoffmann, and N. W. Ashcroft. Benzene under high pressure: A story of molecular crystals transforming to saturated networks, with a possible intermediate metallic phase. *J. Am. Chem. Soc.* **133**, 9023 (2011).
- [88] C. J. Pickard and R. J. Needs. *Ab initio* random structure searching. *J. Condens. Matter Phys.* **23**, 053201 (2011).
- [89] Y. Wang, J. Lv, L. Zhu and Y. Ma. CALYPSO: A method for crystal structure prediction. *Comput. Phys. Commun.* **183**, 2063 (2012).
- [90] D. C. Lonie and E. Zurek. XtalOpt: An open-source evolutionary algorithm for crystal structure prediction. *Comput. Phys. Commun.* **182**, 372 (2011).

- [91] A. R. Oganov and C. W. Glass. Crystal structure prediction using *ab initio* evolutionary techniques: Principles and applications. *J. Chem. Phys.* **124**, 244704 (2006).
- [92] A. R. Oganov, A. O. Lyakhov and M. Valle. How evolutionary crystal structure prediction works and why. *Acc. Chem. Res.* **44**, 227 (2011).
- [93] W. Zhang, A. R. Oganov, A. F. Goncharov, Q. Zhu, S. E. Boulfelfel, A. O. Lyakhov, E. Stavrou, M. Somayazulu, V. B. Prakapenka and Z. Konôpková. Unexpected stable stoichiometries of sodium chlorides. *Science* **342**, 1502 (2013).
- [94] Q. Zhu, A. R. Oganov and A. O. Lyakhov. Novel stable compounds in the Mg-O system under high pressure. *Phys. Chem. Chem. Phys.* **15**, 7696 (2013).
- [95] X. Zhou, A. R. Oganov, G. Qian and Q. Zhu. First-principles determination of the structure of magnesium borohydride. *Phys. Rev. Lett.* **109**, 245503 (2012).
- [96] A. R. Oganov and S. Ono. Theoretical and experimental evidence for a post-perovskite phase of MgSiO<sub>3</sub> in Earth's D'' layer. *Nature* **430**, 445 (2004).
- [97] A. R. Oganov and S. Ono. The high-pressure phase of alumina and implications for Earth's D'' layer. *Proc. Natl. Acad. Sci.* **102**, 10828 (2005).
- [98] N. A. Mahammedi and M. Ferhat. Investigation of the structural, electronic and mechanical properties of type-VIII Ba<sub>8</sub>Si<sub>46</sub> clathrate under high-pressure through first-principles. *Silicon* **12**, 381 (2020).
- [99] R. Dupuis, J. S. Dolado, M. Benoit, J. Sarga and A. Ayuela. Quantum nuclear dynamics of protons within layered hydroxides at high pressure. *Sci. Rep.* **7**, 1 (2017).
- [100] D. Pottmaier, E. R. Pinatel, J. G. Vitillo, S. Garroni, M. Orlova, M. D. Baró, G. B. M. Vaughan, M. Fichtner, W. Lohstroh and M. Baricco. Structure and thermodynamic properties of the NaMgH<sub>3</sub> perovskite: A comprehensive study. *Chem. Mater.* **23**, 2317 (2011).
- [101] W. J. Yin, M. Krack, X. Li, L. Z. Chen and L. M. Liu. Periodic continuum solvation model integrated with first-principles calculations for solid surfaces. *Prog. Nat. Sci.* **27**, 283 (2017).

- [102] H. Öztürk, G. G. Arslan, C. Kürkçü and C. Yamçıçier, Structural phase transformation, intermediate states and electronic properties of PbTe under high pressure. *J. Electron. Mater.* **49**, 1 (2020).
- [103] D. Selli, I. A. Baburin, R. Martoňák and S. Leoni. Novel metastable metallic and semiconducting germaniums. *Sci. Rep.* **3**, 1466 (2013).
- [104] A. Bouibes and A. Zaoui. High-pressure polymorphs of ZnCO<sub>3</sub>: Evolutionary crystal structure prediction. *Sci. Rep.* **4**, 5172 (2014).
- [105] N. Sagatov, P. N. Gavryushkin, T. M. Inerbaev and K. D. Litasov. New high-pressure phases of Fe<sub>7</sub>N<sub>3</sub> and Fe<sub>7</sub>C<sub>3</sub> stable at Earth's core conditions: Evidences for carbon-nitrogen isomorphism in Fe-compounds. *RSC Adv.* **9**, 3577 (2019).
- [106] P. Tsuppayakorn-aek, W. Luo, R. Ahuja and T. Bovornratanaraks. The high-pressure superconducting phase of arsenic. *Sci. Rep.* **8**, 1 (2018).
- [107] J. Zhang, C. Yang, W. Rao, J. Hao and Y. Li, Y. Prediction of high-pressure phases of Weyl semimetal NbAs and NbP. *Sci. Rep.* **7**, 1 (2017).
- [108] P. Avery, X. Wang, C. Oses, E. Gossett, D. M. Proserpio, C. Toher, S. Curtarolo and E. Zurek. Predicting superhard materials via a machine learning informed evolutionary structure search. *Npj Comput. Mater.* **5**, 1 (2019).
- [109] H. C. Kelly and J. O. Edwards. Evidence for the open chain structure of ethane 1, 2-diamineborane. *Inorg. Chem.* **2**, 226 (1963).
- [110] H. C. Kelly and J. O. Edwards. Ethane 1, 2-diamineborane. *J. Am. Chem. Soc.* **82**, 4842 (1960).
- [111] S. Sahler, H. Konnerth, N. Knoblauch and M. H. G. Prechtl. Hydrogen storage in amine boranes: Ionic liquid supported thermal dehydrogenation of ethylene diamine bisborane. *Int. J. Hydrog. Energy* **38**, 3283 (2013).

- [112] F. Leardini, M. J. Valero-Pedraza, E. Perez-Mayoral, R. Cantelli and M. A. Bañares. Thermolytic decomposition of ethane 1,2-diamineborane investigated by thermoanalytical methods and *in situ* vibrational spectroscopy. *J. Phys. Chem. C* **118**, 17221 (2014).
- [113] D. Neiner, A. Karkamkar, M. Bowden, Y. Joon Choi, A. Luedtke, A. J. Holladay, A. Fisher, N. Szymczak and T. Autrey. Kinetic and thermodynamic investigation of hydrogen release from ethane 1,2-di-dmineborane. *Energy Environ. Sci.* **4**, 4187 (2011).
- [114] P. Wang. Pressure tuning of energy storage materials probed by *in-situ* vibrational spectroscopy and synchrotron radiation. *Electronic Thesis and Dissertation Repository* 5823 (2018).
- [115] W. Kohn and L. J. Sham. Self-consistent equations including exchange and correlation effects. *Phys. Rev.* **140**, A1133 (1965).
- [116] D. S. Sholl and J. A. Steckel, in *Density functional theory: A practical introduction*. Hoboken, N.J: Wiley (2009).
- [117] R. G. Parr and W. Yang. Density-functional theory of atoms and molecules. *O. U. P.* (1993).
- [118] U. von Barth and L. Hedin. A local exchange-correlation potential for the spin polarized case. i. *J. Phys. C* **5**, 1629 (1972).
- [119] S. H. Vosko, L. Wilk and M. Nusair. Accurate spin-dependent electron liquid correlation energies for local spin density calculations: A critical analysis. *Can. J. Phys.* **58**, 1200 (1980).
- [120] J. P. Perdew and A. Zunger. Self-interaction correction to density-functional approximations for many-electron systems. *Phys. Rev. B* **23**, 5048 (1981).
- [121] L. A. Cole and J. P. Perdew. Calculated electron affinities of the elements. *Phys. Rev. A* **25**, 1265 (1982).
- [122] J. P. Perdew and Y. Wang. Accurate and simple analytic representation of the electron-gas correlation energy. *Phys. Rev. B* **45**, 13244 (1992).

- [123] J.C. Grossman, L. Mitas and K. Raghavachari. Structure and stability of molecular carbon: Importance of electron correlation. *Phys. Rev. Lett.* **75**, 3870 (1995).
- [124] J. P. Perdew and W. Yue. Accurate and simple density functional for the electronic exchange energy: Generalized gradient approximation. *Phys. Rev. B* **33**, 8800 (1986).
- [125] J. P. Perdew, K. Burke and M. Ernzerhof. Generalized gradient approximation made simple. *Phys. Rev. Lett.* **77**, 3865 (1996).
- [126] J. P. Perdew, A. Ruzsinszky, G. I. Csonka, O. A. Vydrov, G. E. Scuseria, L. A. Constantin, X. Zhou and K. Burke. Restoring the density-gradient expansion for exchange in solids and surfaces. *Phys. Rev. Lett.* **100**, 136406 (2008).
- [127] M. Levy, J. P. Perdew. Tight bound and convexity constraint on the exchange correlation-energy functional in the low-density limit, and other formal tests of generalized-gradient approximations. *Phys. Rev. B* **48**, 11638 (1993).
- [128] X. Wu, P. Jiang, Y. Ding, W. Cai, S.-S. Xie, Z. L. Wang. Mismatch strain induced formation of ZnO/ZnS heterostructured rings. *Adv. Mater.* **19**, 2319 (2007).
- [129] M. Dion, H. Rydberg, E. Schröder, D. C. Langreth and B. I. Lundqvist. Van der Waals density functional for general geometries. *Phys. Rev. Lett.* **92**, 246401 (2004).
- [130] T. Thonhauser, V. R. Cooper, S. Li, A. Puzder, P. Hyldgaard and D. C. Langreth. Van der Waals density functional: Self-consistent potential and the nature of the van der Waals bond. *Phys. Rev. B* **76**, 125112 (2007).
- [131] A. Bil, B. Kolb, R. Atkinson, D. G. Pettifor, T. Thonhauser and A. N. Kolmogorov. Van der Waals interactions in the ground state of  $\text{Mg}(\text{BH}_4)_2$  from density functional theory. *Phys. Rev. B* **83**, 224103 (2011).
- [132] H. J. Monkhorst and J. D. Pack. Special points for Brillouin-zone integrations. *Phys. Rev. B* **13**, 5188 (1976).

- [133] D. Vanderbilt. Soft self-consistent pseudopotentials in a generalized eigenvalue formalism. *Phys. Rev. B* **41**, 7892 (1990).
- [134] E. J. Walter, Opium pseudopotential generation project, <http://opium.sourceforge.net>.
- [135] A. Boultif and D. Louër. Indexing of powder diffraction patterns for low-symmetry lattices by the successive dichotomy method. *J. Appl. Crystallogr.* **24**, 987 (1991).
- [136] R. J. Angel. Equations of state. *Rev. Mineral Geochem.* **41**, 35 (2001).
- [137] R. Custelcean, J. E. Jackson. Dihydrogen bonding: Structures, energetics, and dynamics. *Chem. Rev.* **101**, 1963 (2011).
- [138] M. Hanfland, A. Brillante, A. Girlando and K. Syassen. Raman study of the pressure-induced neutral-to-ionic transition in tetrathiafulvalene chloranil. *Phys. Rev. B* **38**, 1456 (1998).



**Appendix:** Cell parameters ( $a, b, c$  in Å;  $\alpha, \beta, \gamma$  in degrees) and Wyckoff positions for the primitive unit cells of the candidates at ambient pressure. All structures are optimized using the vdW-DF functional.

*Pbca*

a,b,c	10.6691	8.3454	7.1510
$\alpha,\beta,\gamma$	90.000	90.000	90.000
N (8c)	0.6631	0.0847	1.0501
C (8c)	0.5245	0.0564	1.0663
B (8c)	0.7214	0.2030	1.1870
H (8c)	0.6806	0.1312	0.9368
H (8c)	0.7089	0.9765	1.0557
H (8c)	0.5082	0.0066	1.1875
H (8c)	0.4785	0.1735	1.0600
H (8c)	0.6658	0.3301	1.1749
H (8c)	0.7021	0.1404	1.3180
H (8c)	0.8328	0.2161	1.4590

*P2<sub>1</sub>/c (B)*

a,b,c	3.857	10.661	7.151
$\alpha,\beta,\gamma$	90.000	128.300	90.000
N (4e)	0.2093	-0.0952	0.2750
C (4e)	0.2079	-0.0374	0.0867
B (4e)	0.6577	-0.1619	-0.4791
H (4e)	0.6480	-0.1817	0.6419
H (4e)	0.9611	-0.0944	0.5392
H (4e)	0.6830	-0.2572	0.3974
H (4e)	0.1364	-0.0265	0.3479
H (4e)	-0.0387	-0.1613	0.1993
H (4e)	0.2397	-0.1132	-0.0047
H (4e)	0.4921	0.0249	0.1748

*P2<sub>1</sub>/c (A)*

a,b,c	4.7443	6.7049	10.7276
$\alpha,\beta,\gamma$	90.000	103.220	90.000
N (4e)	0.0175	0.2509	1.4125
C (4e)	0.8850	0.4260	1.4654
B (4e)	0.7794	0.0892	1.3379
H (4e)	0.9177	0.9471	1.3139
H (4e)	0.6411	0.1709	1.2426
H (4e)	0.6279	0.0447	1.4108
H (4e)	0.1351	0.3021	1.3495
H (4e)	0.1600	0.1792	1.4855
H (4e)	0.7611	0.3658	0.5314
H (4e)	0.7357	0.4975	1.3847

*C2/c*

a,b,c	10.7230	11.8790	14.2650
$\alpha,\beta,\gamma$	90.000	132.643	90.000
N (8f)	0.5737	0.1620	0.6022
N (8f)	0.1839	-0.0832	0.5749
C (8f)	0.6061	0.2752	0.6638
C (8f)	0.2466	-0.1585	0.6855
B (8f)	0.4052	0.0947	0.5547
B (8f)	0.5390	0.3694	0.4293
H (8f)	0.4353	-0.0057	0.5612
H (8f)	0.2867	0.1233	0.4459
H (8f)	0.3862	0.1201	0.6264
H (8f)	0.5627	0.1730	0.5255
H (8f)	0.6806	0.1139	0.6655
H (8f)	0.6441	0.2584	0.7554
H (8f)	0.4860	0.3211	0.6043
H (8f)	0.3398	-0.2162	0.7024
H (8f)	0.3127	-0.1052	0.7700
H (8f)	0.2871	-0.0594	0.5880
H (8f)	0.1435	-0.0090	0.5840
H (8f)	0.5909	0.2817	0.4228
H (8f)	0.4101	0.3542	0.4088
H (8f)	0.5201	0.4412	0.3600

*P2<sub>1</sub>2<sub>1</sub>2<sub>1</sub> (A)*

a,b,c	4.7538	12.7409	10.5895
$\alpha,\beta,\gamma$	90.000	90.000	90.000
N (4a)	0.5867	0.1339	0.0816
N (4a)	1.4599	0.1122	0.4380
C (4a)	1.4223	0.1192	0.1192
C (4a)	0.6099	0.1389	0.1389
B (4a)	0.4137	0.1251	0.9473
B (4a)	0.6403	0.1249	0.5698
H (4a)	0.4935	0.1967	0.8813
H (4a)	1.1630	0.1311	0.9705
H (4a)	0.4745	0.0424	0.8994
H (4a)	0.6854	0.2058	0.0850
H (4a)	0.7442	0.0786	0.0808
H (4a)	1.3399	0.0389	0.2012
H (4a)	1.2465	0.1745	0.1993
H (4a)	0.6751	0.2212	0.3227
H (4a)	0.7976	0.0893	0.3136
H (4a)	1.3833	0.0370	0.4314
H (4a)	1.2849	0.1595	0.4449
H (4a)	0.8842	0.1049	0.5475
H (4a)	0.6089	0.2146	0.6051
H (4a)	0.5361	0.0641	0.6444

*P2<sub>1</sub>2<sub>1</sub>2<sub>1</sub> (B)*

a,b,c	13.8892	6.2744	7.2586
$\alpha,\beta,\gamma$	90.000	90.000	90.000
N (4a)	0.6874	0.8142	0.2138
N (4a)	0.5568	0.4802	0.5771
C (4a)	0.6130	0.6582	0.2835
C (4a)	0.6378	0.5957	0.4822
B (4a)	0.6726	0.6726	0.2776
B (4a)	0.5758	0.5758	0.7963
H (4a)	0.7516	0.1449	0.2760
H (4a)	0.6379	0.0634	0.4308
H (4a)	0.6191	0.1434	0.1648
H (4a)	0.7548	0.7635	0.2541
H (4a)	0.6888	0.8087	0.0723
H (4a)	0.6114	0.5185	0.1933
H (4a)	0.5429	0.7376	0.2780
H (4a)	0.6531	0.7371	0.5645
H (4a)	0.7011	0.4919	0.4847
H (4a)	0.5435	0.3385	0.5110
H (4a)	0.4958	0.5721	0.5670
H (4a)	0.6228	0.2686	0.8055
H (4a)	0.6185	0.5841	0.8587
H (4a)	0.4976	0.4101	0.8665

$P2_1$ 

a, b, c	9.1175	11.1829	6.2543
$\alpha, \beta, \gamma$	90.000	97.799	90.000
N (2a)	0.3608	0.5829	0.5061
N (2a)	0.3962	0.3905	1.0068
N (2a)	0.1727	0.0757	0.5255
N (2a)	0.0705	0.8884	-0.0021
C (2a)	0.4328	0.5200	0.3352
C (2a)	0.3200	0.4582	0.1671
C (2a)	0.1375	0.9665	0.6509
C (2a)	0.0963	0.0005	0.8729
B (2a)	0.4792	0.6361	0.7037
B (2a)	0.2848	0.3270	0.8150
B (2a)	0.0322	0.1491	0.3968
B (2a)	0.2208	0.8247	0.1213
H (2a)	0.4083	0.6652	0.8447
H (2a)	0.5426	0.7189	0.6315
H (2a)	0.5650	0.5553	0.7610
H (2a)	0.2940	0.6502	0.4357
H (2a)	0.3112	0.8285	0.9984
H (2a)	0.5089	0.4538	0.4182
H (2a)	0.4960	0.5871	0.2585
H (2a)	0.2472	0.5240	0.0770
H (2a)	0.2538	0.3936	0.2446
H (2a)	0.4626	0.3257	0.0866
H (2a)	0.4662	0.4474	0.9398
H (2a)	0.2117	0.2554	0.9001
H (2a)	0.2064	0.4049	0.7243
H (2a)	0.3625	0.2813	0.6952
H (2a)	0.0885	0.2298	0.3056
H (2a)	0.9581	0.1864	0.5282
H (2a)	0.9652	0.0799	0.2701
H (2a)	0.2355	0.1347	0.6259
H (2a)	0.2394	0.0489	0.4145
H (2a)	0.2336	0.9068	0.6703
H (2a)	1.0463	0.9195	0.5541
H (2a)	0.9972	0.0565	0.8564
H (2a)	0.1860	0.0502	0.9677
H (2a)	1.0138	0.8270	0.8952
H (2a)	1.0008	0.9087	0.1085
H (2a)	0.2914	0.5239	0.5694
H (2a)	0.2596	0.8805	0.2851
H (2a)	0.1867	0.7227	0.1581

 $Cc$ 

a,b,c	16.9988	15.1486	5.4413
$\alpha,\beta,\gamma$	90.000	108.341	90.000
N (4a)	0.8496	0.1320	0.7812
N (4a)	0.3225	-0.1197	0.6296
N (4a)	0.6040	-0.1205	0.4146
N (4a)	0.5746	-0.3689	0.5053
C (4a)	0.3091	-0.2829	0.6591
C (4a)	0.3659	-0.2031	0.7535
C (4a)	0.5601	-0.2037	0.4520
C (4a)	0.6153	-0.2844	0.4605
B (4a)	0.8588	0.1148	0.0857
B (4a)	0.3210	-0.0989	0.3324
B (4a)	0.6053	-0.0988	0.1207
B (4a)	0.5670	-0.3855	0.7937
H (4a)	0.4000	-0.3258	0.2127
H (4a)	0.8924	0.0439	0.1401
H (4a)	0.7891	0.1149	0.1036
H (4a)	0.8159	0.0806	0.6763
H (4a)	0.4072	-0.3732	0.7571
H (4a)	0.7521	0.2240	0.7102
H (4a)	0.7931	0.2106	0.4491
H (4a)	0.4225	-0.2089	0.7001
H (4a)	0.3822	-0.1964	0.9632
H (4a)	0.3495	-0.0667	0.7428
H (4a)	0.2626	-0.1202	0.6353
H (4a)	0.3896	-0.0708	0.3464
H (4a)	0.3056	-0.1672	0.2118
H (4a)	0.2664	-0.0449	0.2474
H (4a)	0.6597	-0.0443	0.1445
H (4a)	0.5367	-0.0709	1.0004
H (4a)	0.6212	-0.1666	0.0288
H (4a)	0.5774	-0.0675	0.4764
H (4a)	0.6640	-0.1215	0.5375
H (4a)	0.5025	-0.2080	0.2904
H (4a)	0.5456	-0.1978	0.6328
H (4a)	0.6736	-0.2786	0.6193
H (4a)	0.6290	-0.2906	0.2781
H (4a)	0.1075	0.0793	0.4646
H (4a)	0.5166	-0.3737	0.3700
H (4a)	0.1370	0.1151	0.9461
H (4a)	0.5258	-0.3262	0.8403
H (4a)	0.5337	-0.4565	0.7849

# Curriculum Vitae

Rongfeng Guan

---

## EDUCATION

---

- **University of Western Ontario, London, Canada** **September 2018–Present**  
Master of Science candidate in Chemistry
- **Shenyang University of Chemical Technology, China** **September 2014–June 2018**  
Bachelor of Science in Chemistry

---

## HONORS AND AWARDS

---

- Third-class scholarship October 2015
- Third-class “Baijiaqianyou” scholarship October 2015
- First-class, 2015 College Students’ Innovative Entrepreneurial Training Plan Program  
April 2016
- Second-class scholarship October 2017
- Third-class “Baijiaqianyou” scholarship October 2017
- First-class scholarship April 2018

---

## WORK EXPERIENCE

---

- **Undergraduate research assistant** April 2015–April 2016  
  
**Project:** Study on MOF Thin Films (ZIF-8) *In-situ* Synthesis and Corrosion Resistance on Zinc Alloys Surface

● **Graduate research assistant** September 2018–Present

● **First-year laboratory/ tutorial teaching assistant** September 2018–Present

CHEM 1301A: Discovering Chemical Structure

---

## **GRADUATE COURSES COMPLETED**

---

CHEM 9648A: Computational Quantum Chemistry

CHEM 9444B: Statistical Mechanics and Molecular Simulations